*J. Fluid Mech.* (1984), *vol.* 138, *pp.* 21–52
*Printed in Great Britain*



# Numerical investigation of supercritical Taylor-vortex flow for a wide gap

By H. FASEL† AND O. BOOZ
Institut A für Mechanik, Universität Stuttgart, Stuttgart, Germany

(Received 18 February 1983)

For a wide gap ($R_1/R_2 = 0.5$) and large aspect ratios $L/d$, axisymmetric Taylor-vortex flow has been observed in experiments up to very high supercritical Taylor (or Reynolds) numbers. This axisymmetric Taylor-vortex flow was investigated numerically by solving the Navier–Stokes equations using a very accurate (fourth-order in space) implicit finite-difference method. The high-order accuracy of the numerical method, in combination with large numbers of grid points used in the calculations, yielded accurate and reliable results for large supercritical Taylor numbers of up to $100Ta_c$ (or $10Re_c$). Prior to this study numerical solutions were reported up to only $16Ta_c$. The emphasis of the present paper is placed upon displaying and elaborating the details of the flow field for large supercritical Taylor numbers. The flow field undergoes drastic changes as the Taylor number is increased from just supercritical to $100Ta_c$. Spectral analysis (with respect to $z$) of the flow variables indicates that the number of harmonics contributing substantially to the total solution increases sharply when the Taylor number is raised. The number of relevant harmonics is already unexpectedly high at moderate supercritical $Ta$. For larger Taylor numbers, the evolution of a jetlike or shocklike flow structure can be observed. In the axial plane, boundary layers develop along the inner and outer cylinder walls while the flow in the core region of the Taylor cells behaves in an increasingly inviscid manner.

## 1. Introduction

The pioneering work of Taylor (1923) on the instability of Couette flow between coaxial rotating cylinders has inspired numerous significant investigations, both theoretical and experimental. Using linear stability theory, Taylor determined a condition for stability of Couette flow for the case of a small gap, i.e. he determined a critical Taylor number $Ta_c$. The theoretical calculations were verified convincingly by Taylor's own laboratory experiments, which showed that, with the inner cylinder rotating and the outer cylinder at rest, the instability leads to a secondary motion with cellular toroidal vortices of practically regular spacing in the axial direction.

In the stability theory analysis of subsequent investigators, the small-gap-width limitation was successfully removed to allow for the determination of critical Taylor numbers for large finite gap widths (see e.g. Chandrasekhar 1961; Kirchgässner 1961; Kirchgässner & Sorger 1969; Krylov & Misnik 1963). Kirchgässner (1966) and Velte (1966) (see also Kirchgässner & Sorger) provided rigorous analytical proofs that the critical Taylor number $Ta_c$ is a bifurcation point for the time-independent Navier–Stokes equations and that for $Ta > Ta_c$ two types of steady solutions exist: the Couette flow and the Taylor-vortex flow.

† Present address: University of Arizona, Aerospace and Mechanical Engineering Department, Tucson, AZ 85721.

Using weakly nonlinear analysis, the structure of the supercritical Taylor-vortex motion was calculated by Stuart (1958), Davey (1962), Reynolds & Potter (1967) and Kirchgässner & Sorger (1969). However, these investigations were limited to small gap width and/or small supercritical Taylor numbers. The different approaches taken in computing the supercritical flows and the difficulties involved are discussed in detail in the survey papers by Di Prima & Rogers (1969) and Stuart (1971).

As the Taylor number is increased beyond $Ta_c$ experimental evidence has shown (especially for larger gap widths) that for a given $Ta$ various axial wavelengths are possible. The wavelength observed depends on the preceding time history of evolution to the supercritical state (see e.g. Snyder 1969; Burkhalter & Koschmieder 1975). Thus, beyond $Ta_c$ one is confronted with a problem of non-uniqueness, which has yet to be resolved satisfactorily. From nonlinear stability analysis of the Taylor-vortex motion, Kogelman & Di Prima (1970) and Nakaya (1974) determined subregions of wavenumber space where stable solutions do exist for supercritical Taylor numbers. These subregions can be considerably smaller than the unstable region predicted by linear stability analysis of the Couette flow.

For small gap widths, the supercritical Reynolds number regime in which the axisymmetric vortex motion can be observed experimentally is very small. Indeed, another instability sets in as the Taylor-vortex flow becomes unstable with respect to azimuthal disturbances. This leads to the wavy vortex or the doubly periodic vortex motion, which, in addition to the axial periodicity, is also periodic in time. This instability and the structure of the doubly periodic motion were studied in great detail in experiments by Coles (1965) (see also Schulz-Grunow & Hein 1956; Schwarz, Springett & Donnelly 1964), where particular attention was also given to the question of non-uniqueness. For this case this question is even more difficult to deal with since, for a given Taylor number, the azimuthal wavenumber can also vary. The instability that leads to the wavy vortex motion was investigated theoretically by Davey, Di Prima & Stuart (1968) and later by Eagles (1974) using amplitude expansions for the Taylor-vortex flow up to third and fifth order respectively. By solving the Navier–Stokes equations numerically, Meyer (1969) made an attempt to investigate the stability of the Taylor-vortex flow and to calculate the doubly periodic motion for a case with $R_1/R_2 = 0.8334$. He employed an explicit finite-difference scheme of first-order accuracy in space and time, and used Fourier expansion in the azimuthal direction (retaining only the first mode).

As the gap width is increased, the second instability sets in at higher and higher Taylor numbers. This trend was confirmed in a recent investigation of various gap widths by Jones (1981), who analysed the stability of axisymmetric Taylor-vortex flow with respect to small non-axisymmetric disturbances. In the investigation by Jones, the axisymmetric Taylor-vortex flow was calculated numerically by use of a Galerkin method to solve the Navier–Stokes equations.

In experiments with a gap width of $R_1/R_2 = 0.5$, the singly periodic Taylor-vortex motion exists up to very large Taylor numbers. Snyder & Lambert (1966) report the first appearance of significant azimuthal waviness at $100Ta_c$. However, they suggest that this was probably due to end effects of the cylinders. This interpretation seems to be supported by their observation that the azimuthally varying component is responsible for less than 5% of the total amplitude up to $500Ta_c$. In recent experiments by Park & Donnelly (1980), pure singly periodic motion was observed up to $Ta = 1340000$, which corresponds approximately to $440Ta_c$ or $21Re_c$. Thus, from experimental evidence it is not at all clear if, as the Taylor number is increased, the flow in a wide gap does undergo any transition to the doubly periodic flow before

breakdown occurs to the fully turbulent motion. For a wide gap, the torque dependency on Taylor numbers was investigated experimentally in great detail by Donnelly (1958, see also Donnelly & Simon 1960). Moreover, using a theoretical model assuming the Taylor vortices to consist of an inviscid core surrounded by boundary layers, Batchelor (see Donnelly & Simon 1960) derived a torque relationship that agreed reasonably well with Donnelly's measurements for large Taylor numbers.

However, relatively little is still known to date of the structure of the Taylor-vortex flow in a wide gap at high supercritical Taylor numbers. Theoretical predictions based on weakly nonlinear theories (e.g. Davey 1962) are not valid far from the critical Taylor number. Detailed measurements are also not available to date, and the only evidence concerning the structure of the flow is based on visualization techniques.

Several attempts were made in the past to numerically investigate the singly periodic Taylor-vortex flow by solving the Navier–Stokes equations using digital computers. In most cases, infinite lengths of the cylinders were assumed, and thus, using periodic boundary conditions, the integration domain in the axial direction could be confined to one or two wavelengths (2 or 4 cells) of the expected Taylor-vortex motion. For example, Meyer (1967) developed a finite-difference method with an explicit time-marching procedure to calculate supercritical flows for small gap widths ($R_1/R_2 > 0.8334$) up to $15Ta_c$. Considering the low (first-order) spatial accuracy of the difference method in combination with the relatively small number of grid points used in his study, details of the flow field were possibly not sufficiently resolved at the higher supercritical Taylor numbers. Similar considerations are also likely to be true for the calculations of Strawbridge & Hooper (1968), who also employed a first-order-accurate finite-difference method together with a relatively coarse mesh. The numerical investigations by Meyer also addressed the question of preferred wavelengths. However, it is questionable whether the calculations performed in this context were appropriate. In any case, the implications of the numerical results shown are unclear (see Di Prima & Rogers 1969). For various large gap widths, Liu & Chen (1973) investigated the time evolution of the Taylor-vortex flow when the inner cylinder was impulsively started from rest. Employing an explicit finite-difference method of first-order accuracy in both space dimensions and in time, they reported good qualitative agreement with their experimental observations.

The investigations of Rogers & Beard (1969) were similar in intent to the investigations discussed in this paper. They applied a combination of a Fourier expansion in the axial direction and a second-order-accurate finite-difference approximation for the radial direction to calculate the flow field for a wide gap with $R_1/R_2 = 0.5$. Calculations were performed up to $5Ta_c$, for which 6 Fourier modes were employed. Meyer-Spasche & Keller (1980) devised a method for accurately predicting the bifurcation point from Couette to Taylor-vortex flow; this method is also based on Fourier expansion in the $z$-direction and finite-difference approximations of second-order accuracy in the $r$-direction. They calculated supercritical flows for small and large gap widths; for example, for $R_1/R_2 = 0.5$ they used 8 modes in the $z$-direction and 15 points in the $r$-direction to calculate the flow up to $4Re_c$ ($16Ta_c$).

The present study represents an attempt to investigate numerically details of the singly periodic Taylor-vortex flow in a wide gap with $R_1/R_2 = 0.5$ (and cylinders of infinite lengths) and for supercritical Reynolds numbers considerably larger than those in previous numerical investigations. To this end, a fully implicit finite-difference method was developed for solving the complete Navier–Stokes equations for incompressible axisymmetric flows. With emphasis being placed on reliable simulations of the flow field up to large supercritical Taylor numbers, high accuracy of the numerical

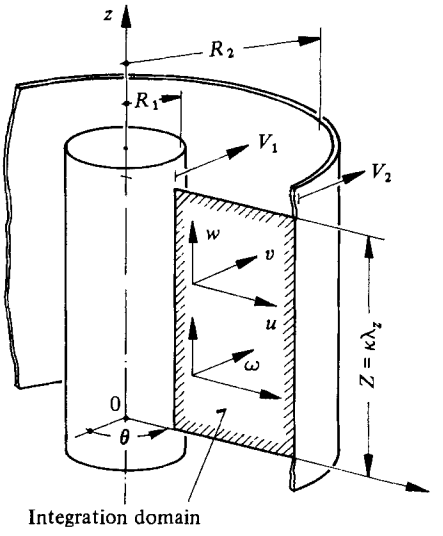


FIGURE 1. Integration domain and notation.

method was of the utmost importance in order to allow for adequate resolution of the ensuing large spatial gradients. To meet this requirement the finite-difference method developed is of fourth-order accuracy with respect to the space dimensions and of second-order accuracy with respect to time. On the basis of extensive test calculations, this accuracy can be considered sufficient to reliably calculate the flow up to about $100Ta_c$ with the computer system available for this study (CD 6600).

In this paper details of the Taylor-vortex motion are presented for a wide range of supercritical Taylor numbers. In particular, the evolution of the flow field as the Taylor number increases up to $100Ta_c$ is elaborated upon. With the fully implicit time-marching procedure employed in the numerical method, realistic simulations of the time-dependent behaviour are also possible.

## 2. Basic equations

Cylindrical coordinates $(r, \theta, z)$ are used in this study. They are shown in figure 1 together with the corresponding velocity components $u, v, w$. Assuming axisymmetric flow, the velocity components are independent of $\theta$. For the case of cylinders of infinite length the integration domain for the numerical model can be reduced to a finite domain $Z$ in the $z$-direction. Using periodicity conditions at the upper and lower boundaries the length $Z$ of the domain is to contain integer multiples of the expected wavelength $\lambda_z$.

For incompressible flows the Navier–Stokes equations can be written in a vorticity–velocity formulation, with a vorticity-transport equation for the vorticity component $\omega$ in the $\theta$-direction (normal to the $(r, z)$-plane), a momentum equation for the velocity component $v$ in the $\theta$-direction, and two Poisson equations for the velocity components in the $r$- and $z$-directions respectively:

$$\frac{\partial\omega}{\partial t}+u\frac{\partial\omega}{\partial r}+w\frac{\partial\omega}{\partial z}-\frac{1}{r}\left(u\omega+2v\frac{\partial v}{\partial z}\right)=\frac{1}{Re}\left(\Delta\omega-\frac{1}{r^2}\omega\right), \tag{1}$$

$$\frac{\partial v}{\partial t}+u\frac{\partial v}{\partial r}+w\frac{\partial v}{\partial z}+\frac{1}{r}uv=\frac{1}{Re}\left(\Delta v-\frac{1}{r^2}v\right), \tag{2}$$

$$\Delta u - \frac{1}{r^2}u = \frac{\partial \omega}{\partial z}, \tag{3}$$

$$\Delta w = -\frac{\partial \omega}{\partial r} - \frac{1}{r}\omega, \tag{4}$$

where the Laplace operator

$$\Delta = \frac{\partial^2}{\partial r^2} + \frac{1}{r}\frac{\partial}{\partial r} + \frac{\partial^2}{\partial z^2}, \tag{5}$$

and the vorticity is defined as

$$\omega = \frac{\partial u}{\partial z} - \frac{\partial w}{\partial r}. \tag{6}$$

The Poisson equations (3) and (4) are derived from the definition of vorticity (6) by differentiation with respect to $z$ and $r$ respectively, and by utilizing the continuity condition

$$\frac{\partial u}{\partial r} + \frac{1}{r}u + \frac{\partial w}{\partial z} = 0. \tag{7}$$

All variables in (1)–(7) are normalized by the radius of the inner cylinder $\bar{R}_1$, the velocity at the inner cylinder $\bar{V}_1$ and the kinematic viscosity $\bar{\nu}$ respectively. The dimensionless quantities relate to their dimensional counterparts, denoted by overbars, as follows:

$$\left.\begin{aligned} r = \frac{\bar{r}}{\bar{R}_1}, \quad z = \frac{\bar{z}}{\bar{R}_1}, \quad t = \frac{t\bar{V}_1}{\bar{R}_1}, \\ u = \frac{\bar{u}}{\bar{V}_1}, \quad w = \frac{\bar{w}}{\bar{V}_1}, \quad v = \frac{\bar{v}}{\bar{V}_1}, \quad \omega = \frac{\bar{R}_1}{\bar{V}_1}\bar{\omega}. \end{aligned}\right\} \tag{8}$$

The Reynolds number is defined as $Re = \bar{V}_1 \bar{R}_1 / \bar{\nu}$.

For the numerical method (an implicit finite-difference method) employed in the present investigation, this formulation has a clear advantage over the primitive variable formulation $(u, v, w, p)$ with regard to computer storage requirements. Since the present formulation consists of only two equations that have time derivatives, in contrast to three equations with time derivatives for the $(u, v, w, p)$ formulation, less storage is required for an implicit time-marching procedure to retain the function values at preceding time levels. Of course, efficient use of available storage is of the utmost importance for investigations such as those intended in this study. This vorticity–velocity formulation is basically the axisymmetric extension of the vorticity–velocity formulation for plane flows which was used for numerical investigations of hydrodynamic stability of plane boundary-layer flows (Fasel 1974, 1976). There, for the plane case, this formulation of the Navier–Stokes equations consists of a vorticity-transport equation and two Poisson equations for the two velocity components.

The system of partial differential equations (1)–(4) together with appropriate boundary conditions is sufficient to determine the vorticity $\omega$ and the velocity components $u, v, w$. If in addition other quantities are desired, they can be calculated after $\omega, u, v, w$ are determined at all grid points. For example, the dynamic pressure may be determined from the Poisson equation

$$\Delta p = -\left(\frac{\partial u}{\partial r}\right)^2 - \left(\frac{u}{r}\right)^2 - \left(\frac{\partial w}{\partial z}\right)^2 - 2\frac{\partial u}{\partial z}\frac{\partial w}{\partial r} + \frac{2}{r}v\frac{\partial v}{\partial r}, \tag{9}$$

where $p = \bar{p}/\bar{\rho}\bar{V}_1^2$. Equation (9) is derived from the momentum equations for the radial and axial direction assuming axisymmetry and using the continuity condition (7).

Also, a stream function, defined for the axisymmetric case by

$$\frac{1}{r}\frac{\partial \psi}{\partial z} = u, \quad -\frac{1}{r}\frac{\partial \psi}{\partial r} = w, \tag{10a,b}$$

can be determined from

$$\frac{\partial^2 \psi}{\partial r^2} - \frac{1}{r}\frac{\partial \psi}{\partial r} + \frac{\partial^2 \psi}{\partial z^2} = r\omega, \tag{11}$$

which is obtained by inserting (10) into the definition of vorticity (6). The quantities on the right-hand sides of (9) and (10) are given at any time-step after solving (1)–(4). Thus, to determine the pressure or stream function requires numerical solutions of simple elliptic equations with appropriate boundary conditions. The boundary conditions are specified in the next paragraph. In principle $p$ and $\psi$ could also be determined by direct numerical integration: $p$, for example, from either of the two momentum equations in the $r$- or $z$-directions and $\psi$ from either (10$a$) or (10$b$). However, such an integration is inaccurate and thus this procedure is inferior to solving the elliptic equations (see Roache 1976).

## 3. Boundary and initial conditions

*Boundary conditions*

At the upper and lower boundaries of the computational domain (see figure 1) periodicity conditions of the form

$$f(r, Z, t) = f(r, 0, t) \tag{12}$$

are imposed, where $f$ represents any of the dependent variables. $Z$ is the height of the integration domain, $Z = k\lambda_z$ for $k = 1, 2, \ldots$ ($\lambda_z$ is the wavelength). In principle, these conditions would be sufficient at the upper and lower boundaries to obtain numerical solutions. However, for practical reasons in representing the results and also in order to accelerate the numerical computations it is advantageous to fix the cell of the expected Taylor flow relative to the integration domain by imposing additionally

$$w(r, 0, t) = 0 \quad \text{and/or} \quad \omega(r, 0, t) = 0. \tag{13}$$

These additional conditions are only valid if the cell boundaries of the Taylor vortex flow are plane and perpendicular to the $z$-axis. This assumption is consistent not only with experimental observations for the singly periodic flow but also with results of our calculations for which only the periodicity conditions (9) were imposed.

At the walls of the cylinders, $r = R_1$ and $r = R_2$, the velocity components are

$$\left.\begin{aligned} u(r, z, t) &= 0 \quad (r = R_1, R_2), \\ w(r, z, t) &= 0 \quad (r = R_1, R_2), \\ v(r, z, t) &= V_1(t) \quad (r = R_1), \\ &= 0 \quad (r = R_2), \end{aligned}\right\} \tag{14}$$

as only the case with the inner cylinder rotating and the outer cylinder at rest is considered here. The vorticity at the walls of the inner and outer cylinders is calculated from

$$\omega(r, z, t) = -\left.\frac{\partial w}{\partial r}\right|_r \quad (r = R_1, R_2). \tag{15}$$

*Boundary conditions for the calculation of pressure and stream function*

For calculating the pressure by solving the Poisson equation (9), the following boundary conditions of the von Neumann type are used at cylinder walls:

$$\left.\begin{aligned} \frac{\partial p}{\partial r} &= \frac{1}{Re}\frac{\partial^2 u}{\partial r^2}+\frac{1}{R_1}V_1^2 \quad (r = R_1), \\ \frac{\partial p}{\partial r} &= \frac{1}{Re}\frac{\partial^2 u}{\partial r^2} \quad (r = R_2). \end{aligned}\right\} \tag{16}$$

They are obtained from the momentum equation in the $r$-direction. For calculating $\psi$ from (11), a boundary condition for $\psi$ at the cylinder walls is readily obtained from (10) as

$$\psi = \text{constant} \quad (r = R_1, R_2), \tag{17}$$

where, for convenience, the constant can be set equal to zero.

*Initial conditions*

For a calculation of unsteady flows, the flow field at $t = 0$ is given by specifying the initial values of the velocity components $u, v, w$ and of the vorticity $\omega$ in the entire domain and on the boundaries

$$\left.\begin{aligned} u(r,z,0) &= u^0(r,z), \quad v(r,z,0) = v^0(r,z), \\ w(r,z,0) &= w^0(r,z), \quad \omega(r,z,0) = \omega^0(r,z) \end{aligned}\right\} \quad (0 \leqslant z < Z,\ R_1 \leqslant r \leqslant R_2). \tag{18}$$

## 4. Numerical method

For the solution of the governing equations (1)–(4) together with boundary and initial conditions (12–18) a fully implicit finite-difference method was developed. The full implicitness means that all difference approximations and function values, for both governing equations and boundary conditions, are evaluated at the most recent time level. The decision to adopt a fully implicit method instead of a partially implicit or an explicit approach, was influenced by successful attempts with a fully implicit method to investigate hydrodynamic stability of a plane Blasius boundary layer (Fasel 1976). The numerical method used for the present investigations represents a straightforward extension of the previous method for plane flows to axisymmetric flows.

The computational grid and notation used in the method here are shown in figure 2. $M$ and $N$ denote the number of grid points in the $r$- and $z$-directions respectively, $\Delta r$ and $\Delta z$ are the grid spacings of the uniform grid. The coordinates of the grid points are given by

$$\left.\begin{aligned} r &= R_1+(m-1)\,\Delta r \quad (m = 1, 2, \ldots, M), \\ z &= (n-1)\,\Delta z \quad (n = 1, 2, \ldots, N), \\ t &= l\Delta t \quad (l = 0, 1, 2, \ldots). \end{aligned}\right\} \tag{19}$$

For the approximation of the time derivatives, the following 3-point backward difference,

$$\left.\frac{\partial \omega}{\partial t}\right|^l = \frac{1}{2\Delta t}(3\omega^l - 4\omega^{l-1}+\omega^{l-2})+O(\Delta t^2), \tag{20}$$

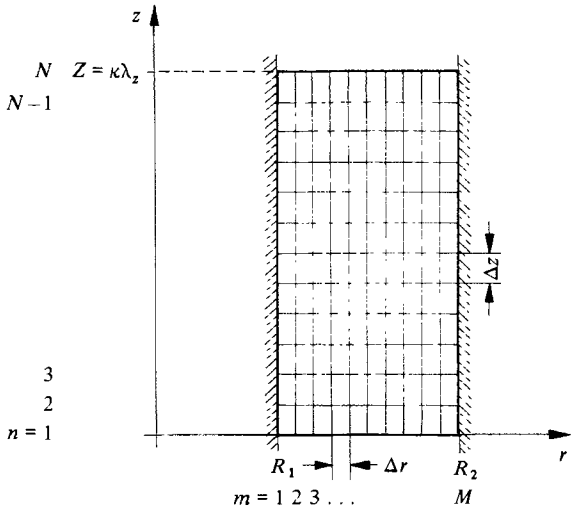


FIGURE 2. Computational mesh.

and an analogous one for $v$, are employed, which lead to a 3-level method. Because of the fully implicit treatment (the velocity components in the convective terms are also taken at the most recent time level) the second-order accuracy in time is retained, and thus realistic time-dependent behaviour may be simulated. For the approximation of the space derivatives the fourth-order-accurate central-difference approximations

$$\left.\begin{aligned} \left.\frac{\partial\omega}{\partial r}\right|_m &= \frac{1}{12\Delta r}(\omega_{m-2}-8\omega_{m-1}+8\omega_{m+1}-\omega_{m+2})+O(\Delta r^4), \\ \left.\frac{\partial^2\omega}{\partial r^2}\right|_m &= \frac{1}{12\Delta r^2}(-\omega_{m-2}+16\omega_{m-1}-30\omega_m+16\omega_{m+1}-\omega_{m+2})+O(\Delta r^4) \end{aligned}\right\} \tag{21}$$

are used for all variables and in both space dimensions throughout the computational domain, except for the grid points on the two grid lines immediately adjacent to the cylinder walls. In the calculation of vorticity at the walls, special treatment is required for these grid points to maintain overall fourth-order accuracy and consistency of the finite-difference formulation.

The systems of equations resulting from the fully implicit approach are coupled with each other via the nonlinear terms in the vorticity-transport equation and the momentum equation; in addition they are coupled by the relationship (15) used for calculating vorticity at the cylinder walls. For the solution of this coupled system of equations a line-iteration procedure similar to the one described by Fasel (1974, 1976) was developed. Here the line iteration is organized such that function values on grid lines parallel to the $r$-axis are determined by a direct-elimination procedure while proceeding iteratively in the $z$-direction. For the direct-elimination procedure the matrices involved are essentially pentadiagonal. Exceptions are the matrix elements resulting from the gridpoints at the wall and the two gridpoints adjacent to the wall. Because of the calculation of vorticity at the walls from (15), the equation system resulting from the vorticity-transport equation (1) is coupled with the system resulting from the Poisson equation (4) for $w$, and therefore the coupled systems have to be solved simultaneously. Possible decoupling of the two systems by taking the right-hand side of (15) at previous iteration levels (lagging) results in extremely poor

convergence behaviour of the entire line-iteration procedure. For the solution of the coupled pentadiagonal system an effective algorithm was developed, which is essentially an extension of the algorithm for coupled tridiagonal systems that was employed previously (Fasel 1974, 1976). For details of the numerical method see Booz (1980).

## 5. Numerical results

With the results presented here it is intended to provide details of the flow fields with emphasis on the changes of the flow when the Reynolds number is increased to large supercritical values. All results are for the case of a wide gap with $R_1/R_2 = 0.5$; thus $Ta = \frac{64}{9}Re^2$. For these calculations the wavelength was fixed at $\lambda_z = 2.0$, which is approximately the wavelength at the critical Reynolds number; Davey (1962), for example, obtained $\lambda_{z_c} = 1.987$, Kirchgässner & Sorger (1969) found $\lambda_{z_c} = 2.094$, and the experimental investigations of Donnelly & Fultz yielded $\lambda_{z_c} = 2.03$.

One could argue that keeping the wavelength fixed may impose too large a constraint on such numerical simulations. However, as observed in experiments (Snyder & Lambert 1966) with an apparatus of aspect ratio $L/d \approx 30$, the wavelength was practically constant and equal to the critical wavelength up to $10Ta_c$. At $100Ta_c$ it differed from $\lambda_c$ only by 10 %. In the experiments of Burkhalter & Koschmieder (1979), also with $L/d \approx 30$, the wavelength remained constant up to $Ta = 80$ when the Taylor number was increased in a quasi-steady manner. On the basis of their experimental evidence, Burkhalter & Koschmieder concluded that the change of wavelength for larger Taylor numbers is caused by end effects, and for infinitely long cylinders the wavelength would not vary with Taylor number as long as the flow is singly periodic.

In the present investigation, calculations were carried out starting with Reynolds numbers below the critical Reynolds number $Re_c = 68.19$ and then increasing the Reynolds number up to $Re_c = 690$, i.e. to more than $10Re_c$ or $100Ta_c$. The integration domain in the $z$-direction comprised two wavelengths for calculations with Reynolds numbers up to 400 and one wavelength for Reynolds numbers larger than 400. The number of grid points used in the calculations, for example at $Re = 80$, was $N_{\lambda_z} = 29$ (points per wavelength in the $z$-direction) and $M = 31$ (points in the $r$-direction). With increasing $Re$, higher and higher accuracy is required, and therefore the number of grid points had to be increased accordingly.

In order to obtain an indication of how the number of grid points should be adjusted, so-called 'convergence' studies were performed, where for identical cases (i.e. identical Reynolds numbers, etc.) solutions were calculated for various numbers of grid points. Typical results of such calculations for $Re = 80$ and $Re = 200$ are shown in figure 3. There the azimuthal velocity component $v$ for $r = \frac{1}{2}(R_1 + R_2)$ (middle of the gap) and $z = 0$ as well as the torque at the inner and outer cylinders are plotted versus the number of grid points $M$ in the $r$-direction for fixed $N_{\lambda_z}$, and versus $N_{\lambda_z}$ for fixed $M$. It is obvious that, with increasing $M$ and $N_{\lambda_z}$ respectively, the solutions asymptotically approach constant values. To obtain a quantitative indication of the deviation from the solution when smaller $M$ and $N_{\lambda_z}$ are used in the computation, the relative deviation of 0.1 % is marked in these plots with symbols –○– and △. The location of the symbol –○– indicates the value upon which the relative change is based. The vertical dotted lines in figure 3 indicate the values of $M$ and $N_{\lambda_z}$ respectively that were finally adopted for the convergence calculations for which the results are shown. Comparison of the curves in figure 3 for $Re = 80$ and $Re = 200$

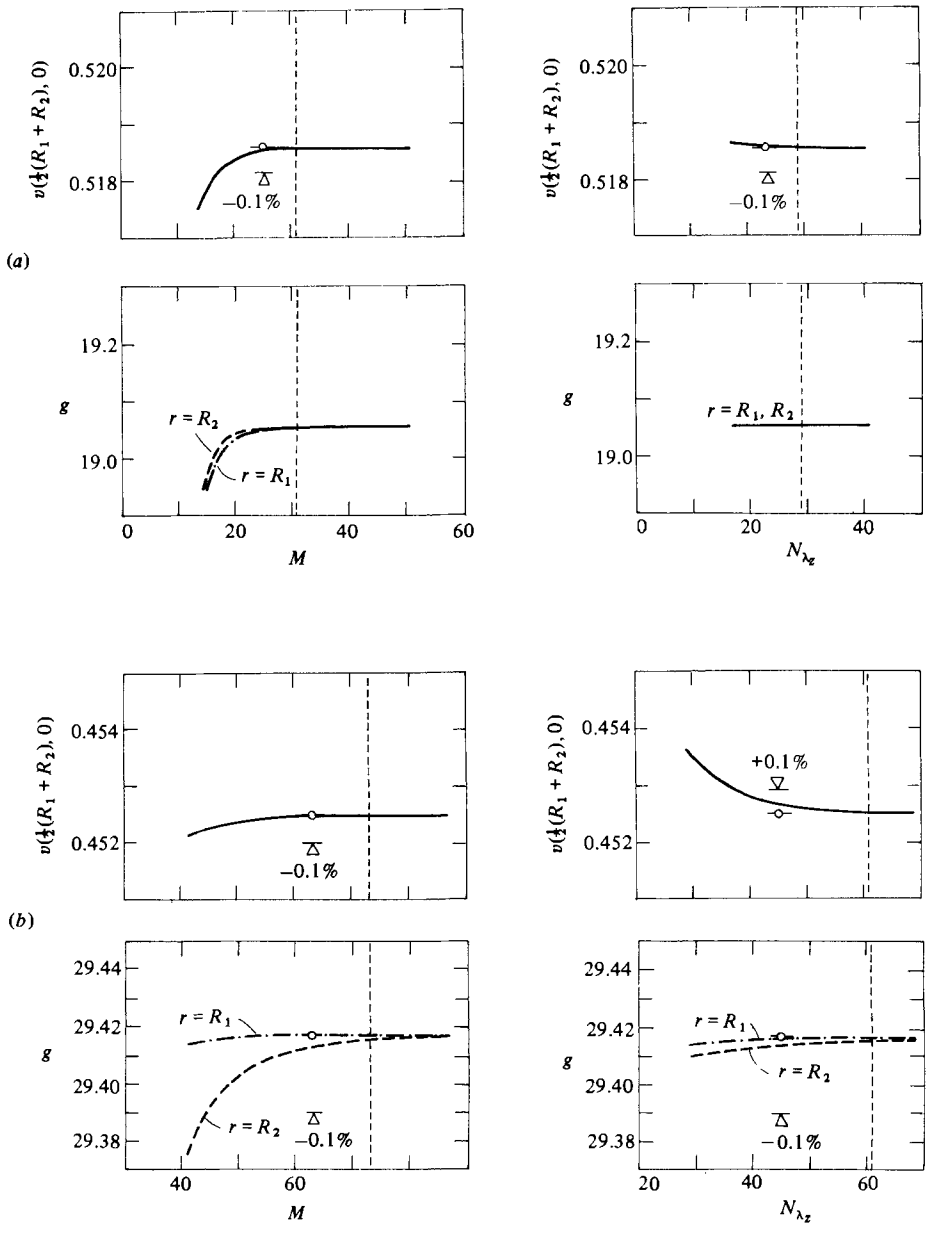


FIGURE 3. Dependence of numerical results on number of grid points used in the computation; for $v$ in the middle of the gap and torque $g$ at $r = R_1$ and $r = R_2$. $M$ = number of grid points in $r$-direction; $N_{\lambda_z}$ = number of grid points per wavelength in $z$-direction. (*a*) $Re = 80$; (*b*) $Re = 200$.

indicates how the demand for accuracy, i.e. for more grid points, increases with larger Reynolds numbers. From convergence studies of this sort it was also learned that the difference of the torque between inner and outer cylinders (as seen in figure 3) is a very good measure of the quality of the spatial resolution, i.e. of whether the number of grid points is sufficient or not. For the results discussed in this paper, the

numbers of grid points used in the calculations were as follows:

$$\begin{aligned} \text{for} \quad 60.0 \leqslant Re \leqslant 72.5: &\quad M = 31, \quad N_{\lambda_z} = 25; \\ 72.5 \leqslant Re \leqslant 100: &\quad M = 33, \quad N_{\lambda_z} = 29; \\ 100 \leqslant Re \leqslant 425: &\quad M = 73, \quad N_{\lambda_z} = 61; \\ 425 \leqslant Re \leqslant 650: &\quad M = 97, \quad N_{\lambda_z} = 81. \end{aligned}$$

With these numbers of grid points, the relative deviation of the torque between inner and outer cylinder was always less than 0.35 % (see table 1) and therefore, the results can be considered extremely reliable and accurate.

### 5.1. *Torque; critical Reynolds number*

In figure 4 the torque obtained from the Navier–Stokes calculations is plotted versus $Re$. It is compared with the experimental measurements of Donnelly (1958) and the stability calculations by Davey (1962), as well as with the theoretical torque relationship by Batchelor (see Donnelly & Simon 1960). Here the torque (denoted by $g$) has been non-dimensionalized by the reference torque $\bar{G} = \bar{\nu}\bar{\rho}\bar{V}_1\bar{R}_1\bar{L}$ ($\bar{L}$ is the length of the cylinders). To facilitate detailed comparison of our numerical results with theoretical predictions, the torque data are also displayed in tabular form. In tables 1 and 2 the calculated torque at the inner and outer cylinder and the relative deviation between inner and outer cylinder are shown, together with the theoretical data by Davey and Batchelor. In the low supercritical Reynolds-number regime (which is plotted on an enlarged scale in figure 4*a*) the agreement with both Davey's and Donnelly's data is extraordinary, except for the deviation near the critical Reynolds number of both Davey's and our results from the experimental data. This is probably due to experimental uncertainties, as it has been demonstrated that end effects (due to finite-length cylinders) and eccentricity (Cole 1976) can affect the transition from Couette to Taylor-vortex flow.

For Reynolds numbers larger than approximately 75 (see figure 4*a*, table 1), our Navier–Stokes solutions slightly overpredict the experimentally determined torque. Davey's results slightly underpredict the torque, and the deviation increases with larger Reynolds numbers. This is, of course, not surprising since Davey's analysis is based on expansions about the critical Reynolds number, and is therefore valid in a strict sense only for small supercritical Reynolds numbers. With this in mind the relatively good agreement of the torque predicted by Davey with our Navier–Stokes results and experimental data is even more remarkable.

The slight but consistent deviation of the numerically determined torque (Navier–Stokes solutions) from the experimental measurements increases with larger $Re$, as seen in figure 4(*b*). There the torque is plotted and compared with experimental data for the entire Reynolds-number regime for which Navier–Stokes solutions have been obtained. This consistent and increasing overprediction of the torque seems at first glance to suggest insufficient spatial resolution to accommodate the larger gradients that arise when $Re$ is raised. However, as is evident from figure 3, if the resolution were insufficient (which is doubtful; see the introductory remarks of §5), increasing the resolution, i.e. increasing the number of grid points in a calculation at a given Reynolds number, would lead to even slightly higher torque values. Thus the deviation between the numerically predicted and experimental torque cannot be explained by a possible lack of resolution in our calculations. It appears rather to be due to the experimental procedure. One possible explanation is that the axial

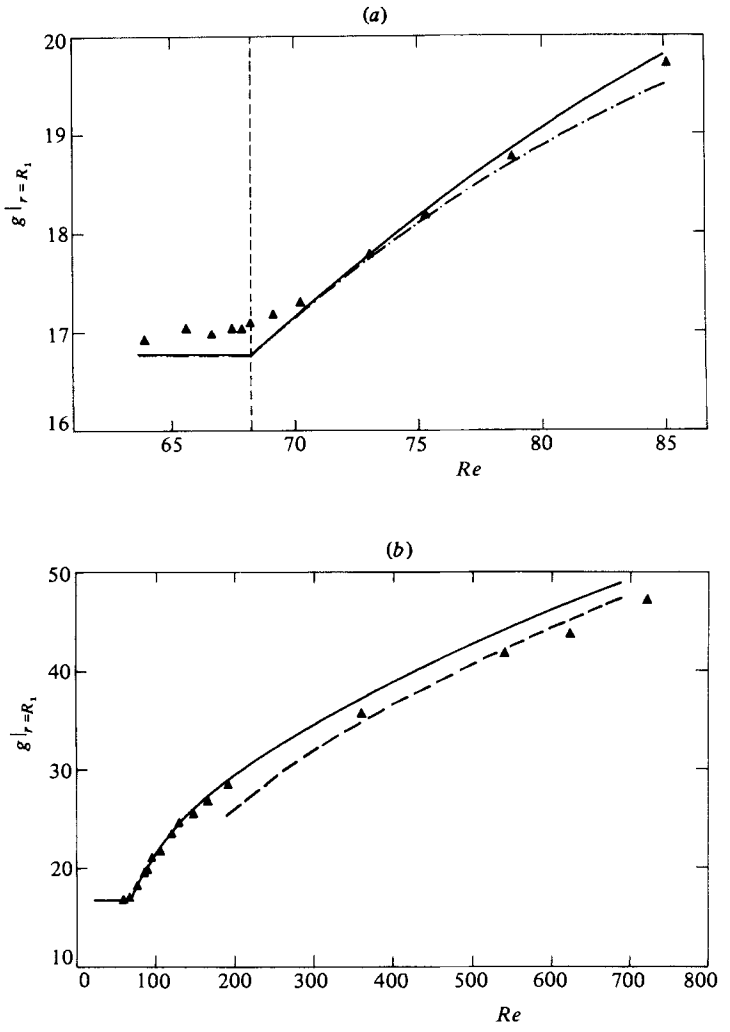


FIGURE 4. Variation of torque with Reynolds number: ▲, experiments (Donnelly 1958); —·—·—, stability theory (Davey 1962); – – – –, theory (Batchelor; see Donnelly & Simon 1960); ———, present (Navier–Stokes solution). (*a*) $Re = 60 \rightarrow 85$; (*b*) $Re = 30 \rightarrow 690$.

wavelength did change slightly in the experiments as the Reynolds number was increased, possibly because of end effects. As observed by Burkhalter & Koschmieder (1975), the end cells grow with increasing Reynolds number. The torque measurements of Donnelly were obtained with an aspect ratio $L/d$ of about 10, which was fixed over the entire Reynolds-number range. With such a relatively small aspect ratio, the effect of the growing end cells on the remaining vortex cells is obviously much stronger than for a larger $L/d$; see, for example, the experiments of Burkhalter & Koschmieder (1975) with a much larger $L/d$ of about 30.

In figure 4 (*b*) (and table 2) the torque obtained from our Navier–Stokes calculations is compared also with the theoretical torque relationship derived by Batchelor (see Donnelly & Simon 1960). This relationship is obtained from a simplified flow model assuming that Taylor cells consist of an inviscid core surrounded by boundary layers. Using these assumptions, Batchelor found that the scaling law

| Reynolds number $\frac{V_1 R_1}{\nu}$ | Torque, inner cylinder $g_1$ | Torque, outer cylinder $g_2$ | Relative deviation $\frac{g_1 - g_2}{g_1} \times 10^3$ | Torque, theoretical (Davey) |
|---|---|---|---|---|
| 60.0 | 16.7551 | 16.7552 | −0.0060 | 16.7552 |
| 65.0 | 16.7551 | 16.7552 | −0.0060 | 16.7552 |
| 67.5 | 16.7551 | 16.7551 | −0.0060 | 16.7552 |
| 68.0 | 16.7551 | 16.7552 | −0.0060 | 16.7552 |
| 69.0 | 16.9347 | 16.9348 | −0.0059 | 16.9382 |
| 70.0 | 17.1537 | 17.1538 | −0.0058 | 17.1544 |
| 72.5 | 17.6752 | 17.6753 | −0.0057 | 17.6563 |
| 75.0 | 18.1627 | 18.1628 | −0.0055 | 18.1089 |
| 77.5 | 18.6208 | 18.6208 | 0.0000 | 18.5184 |
| 80.0 | 19.0527 | 19.0527 | 0.0000 | 18.8900 |
| 82.5 | 19.4613 | 19.4613 | 0.0000 | 19.2285 |
| 85.0 | 19.8490 | 19.8488 | 0.0101 | 19.5375 |
| 87.5 | 20.2177 | 20.2173 | 0.0198 | 19.8204 |
| 90.0 | 20.5692 | 20.5685 | 0.0340 | 20.0800 |
| 92.5 | 20.9051 | 20.9041 | 0.0478 | 20.3189 |
| 95.0 | 21.2267 | 21.2253 | 0.0660 | 20.5391 |
| 97.5 | 21.5352 | 21.5333 | 0.0882 | 20.7427 |
| 100.0 | 21.8318 | 21.8294 | 0.1099 | 20.9312 |

TABLE 1. Dependence of the torque at the inner and outer cylinder on Reynolds number, and comparison with stability theory by Davey (1962)

$\bar{G} \sim \overline{Lp}\, \bar{V}_1^2 \bar{R}_1^2 (Re)^{-\frac{1}{2}}$ for the (dimensional) torque. For the non-dimensional quantities used in the present investigation, this implies that $g = c\, Re^{\frac{1}{2}}$, where $c$ is a constant. As the theoretical relationship is strictly valid for $R \to \infty$, the constant $c$ should be determined at very large Reynolds numbers. However, numerical results are only available for Reynolds numbers up to 690, and therefore any approach in determining the constant is somewhat arbitrary. Here the constant was estimated by extrapolating the asymptotic behaviour which can be observed when plotting $g/Re^{\frac{1}{2}}$ versus $1/Re$. From this, $c$ was estimated to be in the range between 1.75 and 1.85. For the comparison in figure 4(*b*) and table 2, the value chosen for $c$ was 1.8. With this, the agreement of our Navier–Stokes data with the theoretical torque relationship is very reasonable, especially when considering the difficulties in determining the constant $c$ and when considering the assumptions and approximations upon which the theoretical model is based.

Our numerical calculations also clearly indicate that the critical Reynolds number is between 68 and 69. For $Re = 68$ no Taylor vortices arise, no matter how many iterations for the solution of the difference equations are carried out. Even when disturbances that resemble the Taylor-vortex structure are introduced, they quickly disappear. On the other hand, for $Re = 69$, Taylor vortices do quickly appear during the course of iteration. The critical Reynolds number could be pinpointed more accurately by repeating calculations between $Re = 68$ and $Re = 69$ and by placing the critical point between finer and finer Reynolds-number intervals. However, as the main objective of our numerical simulations was a detailed investigation of the flow fields for large supercritical Reynolds numbers, this was not pursued any further. Besides, $Re_c$ can be determined much more inexpensively by stability theory analysis (Davey 1962). On the other hand, a simple extrapolation of the torque curves for the

| Reynolds number $\frac{V_1 R_1}{\nu}$ | Torque, inner cylinder $g_1$ | Torque, outer cylinder $g_2$ | Relative deviation $\frac{g_1-g_2}{g_1}\times 10^3$ | Torque, theoretical (Batchelor) |
|---|---|---|---|---|
| 100 | 21.8352 | 21.8360 | −0.0366 | 18.00 |
| 125 | 24.3199 | 24.3201 | −0.0082 | 20.12 |
| 150 | 26.2646 | 26.2647 | −0.0038 | 22.05 |
| 175 | 27.9276 | 27.9272 | −0.0143 | 23.81 |
| 200 | 29.4266 | 29.4252 | 0.0476 | 25.46 |
| 225 | 30.8195 | 30.8154 | 0.1330 | 27.00 |
| 250 | 32.1351 | 32.1285 | 0.2054 | 28.46 |
| 275 | 33.3899 | 33.3788 | 0.3324 | 29.85 |
| 300 | 34.5931 | 34.5757 | 0.5030 | 31.18 |
| 325 | 35.7512 | 35.7252 | 0.7272 | 32.45 |
| 350 | 36.8685 | 36.8310 | 1.0171 | 33.67 |
| 375 | 37.9486 | 37.8960 | 1.3861 | 34.86 |
| 400 | 38.9943 | 38.9227 | 1.8362 | 36.00 |
| 425 | 40.0052 | 39.9750 | 0.7549 | 37.11 |
| 450 | 40.9887 | 40.9562 | 0.7929 | 38.18 |
| 475 | 41.9441 | 41.9024 | 0.9942 | 39.23 |
| 500 | 42.8736 | 42.8207 | 1.2339 | 40.25 |
| 525 | 43.7788 | 43.7127 | 1.5099 | 41.24 |
| 550 | 44.6614 | 44.5798 | 1.8271 | 42.21 |
| 575 | 45.5228 | 45.4231 | 2.1901 | 43.16 |
| 600 | 46.3642 | 46.2438 | 2.5968 | 44.09 |
| 625 | 47.1867 | 47.0428 | 3.0496 | 45.00 |
| 650 | 47.9907 | 47.8236 | 3.4819 | 45.89 |

TABLE 2. Dependence of the torque at the inner and outer cylinder on Reynolds number and comparison with theory by Batchelor (see Donnelly & Simon 1960)

Couette and for the Taylor flow (see figure 4*a*) leads to an intersection with a critical Reynolds number of 68.2, which is in excellent agreement with the value of 68.18 determined by Davey.

### 5.2. *Details of flow field*

After comparison of the calculated torque with the experimentally determined torque, a global quantity that can be readily measured, results are presented subsequently for other quantities which are more difficult to obtain experimentally and are thus not yet available. First, in figure 5 the radial and azimuthal velocity components for $Re = 72.5$ and $Re = 80$ are compared with corresponding curves obtained from stability analysis by Davey. For $Re = 72.5$ the stability theory and Navier–Stokes results agree quite well near the inner and outer cylinder walls, while slight deviations exist towards the middle of the gap. For $Re = 80$ the deviations in the middle of the gap become considerable, while agreement is still quite reasonable close to the cylinder walls. In particular, the slopes of the curves at $r = R_1$ and $r = R_2$ are almost identical. This explains why the torque of stability theory and of the Navier–Stokes equations in figure 4(*a*) can still be in good agreement up to larger Reynolds numbers, although details of the flow may already differ significantly.

Of course, the difference between stability theory and the Navier–Stokes results would increase continuously with larger Reynolds numbers and, therefore, no further comparison for larger $Re$ is made. Instead, in figure 6 results of our calculations for

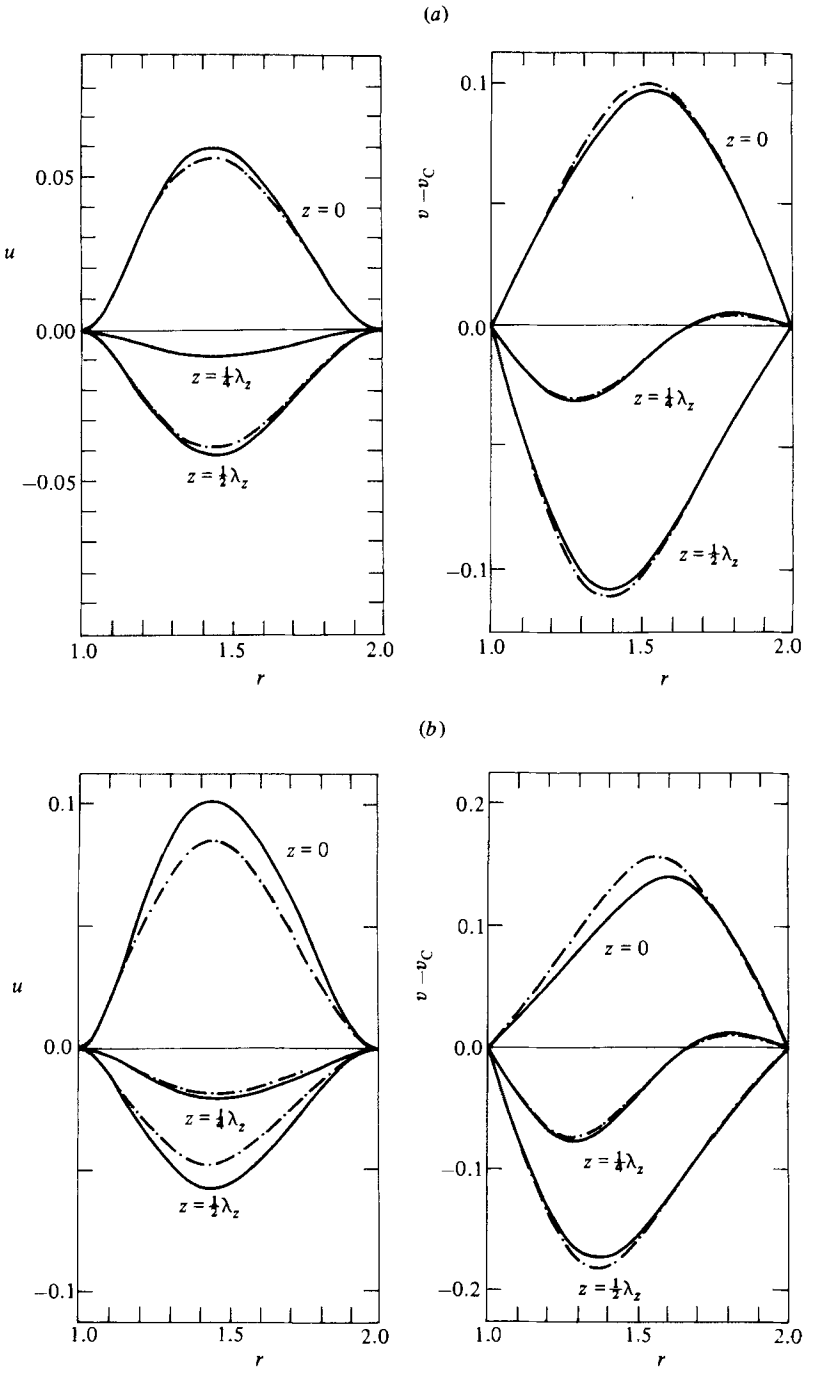


FIGURE 5. Velocity components $u$ and $v$ across the gap for different $z$-locations; comparison with stability theory: —·—·—, stability theory (Davey 1962); ——, present (Navier–Stokes solution); (*a*) $Re = 72.5$; (*b*) $Re = 80$.

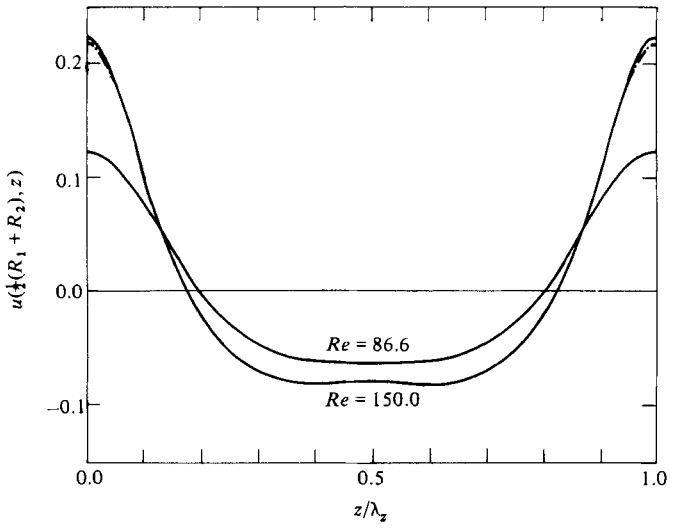


FIGURE 6. Velocity component $u$ at centre of gap versus $z$ for Reynolds numbers $Re = 86.6$ and $Re = 150$. Comparison with other Navier–Stokes solution (Rogers & Beard 1962): —·—·—, Rogers & Beard (1962); ———, present.

the radial velocity component versus $z$ are compared with those of Rogers & Beard (1969). For $Re = 86.6$ the curves practically coincide. At $Re = 150$, which is the highest Reynolds number for which Rogers & Beard computed results, there is only an extremely small deviation, near $z/\lambda_z = 0$ and 1 (cell boundaries). This may be a possible hint that already at this relatively low Reynolds number the limited number of Fourier components used in the calculation of Rogers & Beard starts to have an effect on the numerical solutions (see discussion in §5.3).

The change of the flow field with increasing Reynolds numbers is portrayed in the isoline plots of figure 7. There, lines of constant $\psi$, $\omega$, $u$, $v$ and $p$ are plotted for one wavelength $\lambda_z$ (two cells) and for four representative Reynolds numbers: $Re = 75$, 150, 300 and 600. It is obvious that the intensity of the vortices grows strongly with increasing $Re$ (the increments used in the contour plots were identical for all Reynolds numbers except in the contour plots for $\omega$). This is best observed in the plots of $\psi$ and $\omega$ in figures 7($a$, $b$). Apart from the increase in intensity, a major restructuring of the flow field is taking place. For example the stream function pattern loses its symmetry with respect to a vertical and horizontal axis through the cell centre; this symmetry is only present near the critical Reynolds number. First, the centres (extrema) of the streamline patterns are displaced from the cell centre and are shifted towards the cell boundaries $z/\lambda_z = 0$ and 1. Then, at even higher Reynolds numbers, the centres of the pattern move additionally towards the outer cylinder wall. Associated with this shift of the streamline pattern is the increasing concentration of vorticity at the outer cylinder wall and the displacement of the local extrema (maxima and minima) towards the corners of the cells (figure 7$b$). In contrast with the vorticity build-up near the cylinder walls and near $z/\lambda_z = 0$ and 1, the region between the two cells, near $z/\lambda_z = 0.5$, which is practically void of vorticity, increases strongly in area for larger $Re$.

This build-up of intensity of the secondary flow when $Re$ is increased and the change in patterns just described reflects the evolution of a jetlike (or shocklike) structure in the axial plane which was observed in experiments (Snyder & Lambert 1966;

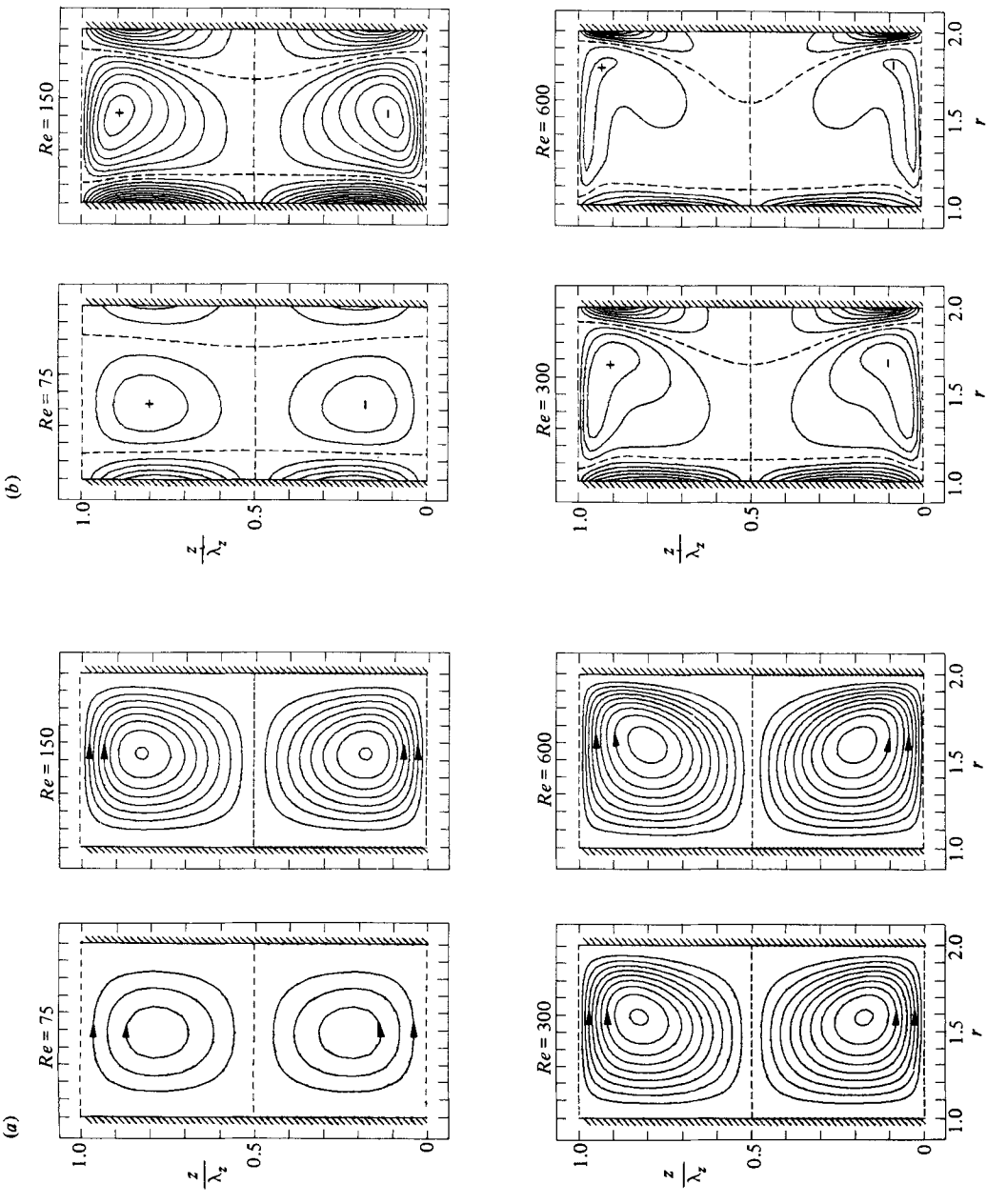


FIGURE 7 (*a*, *b*). For caption see p. 39.

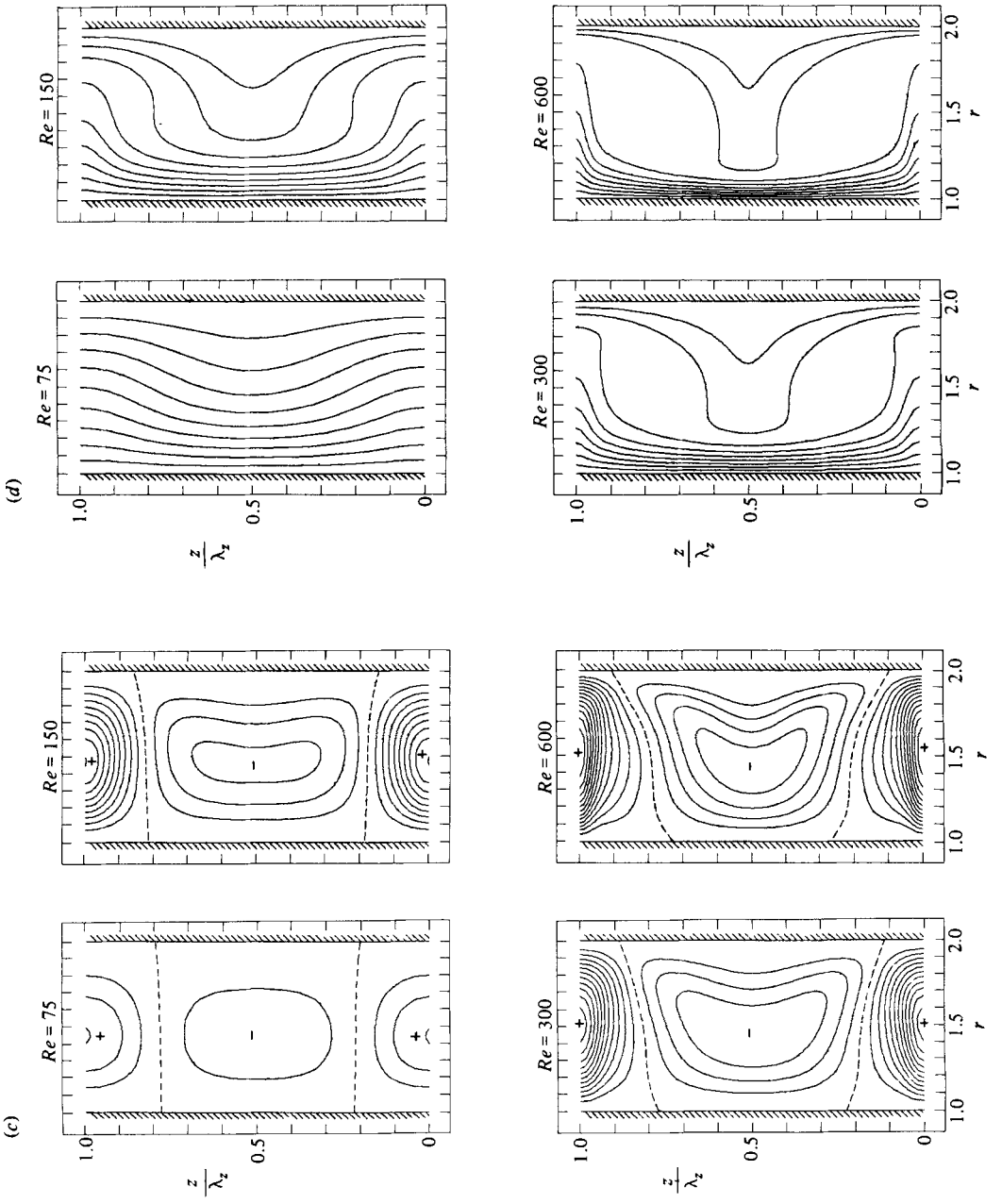


FIGURE 7 (c, d). For caption see facing page.

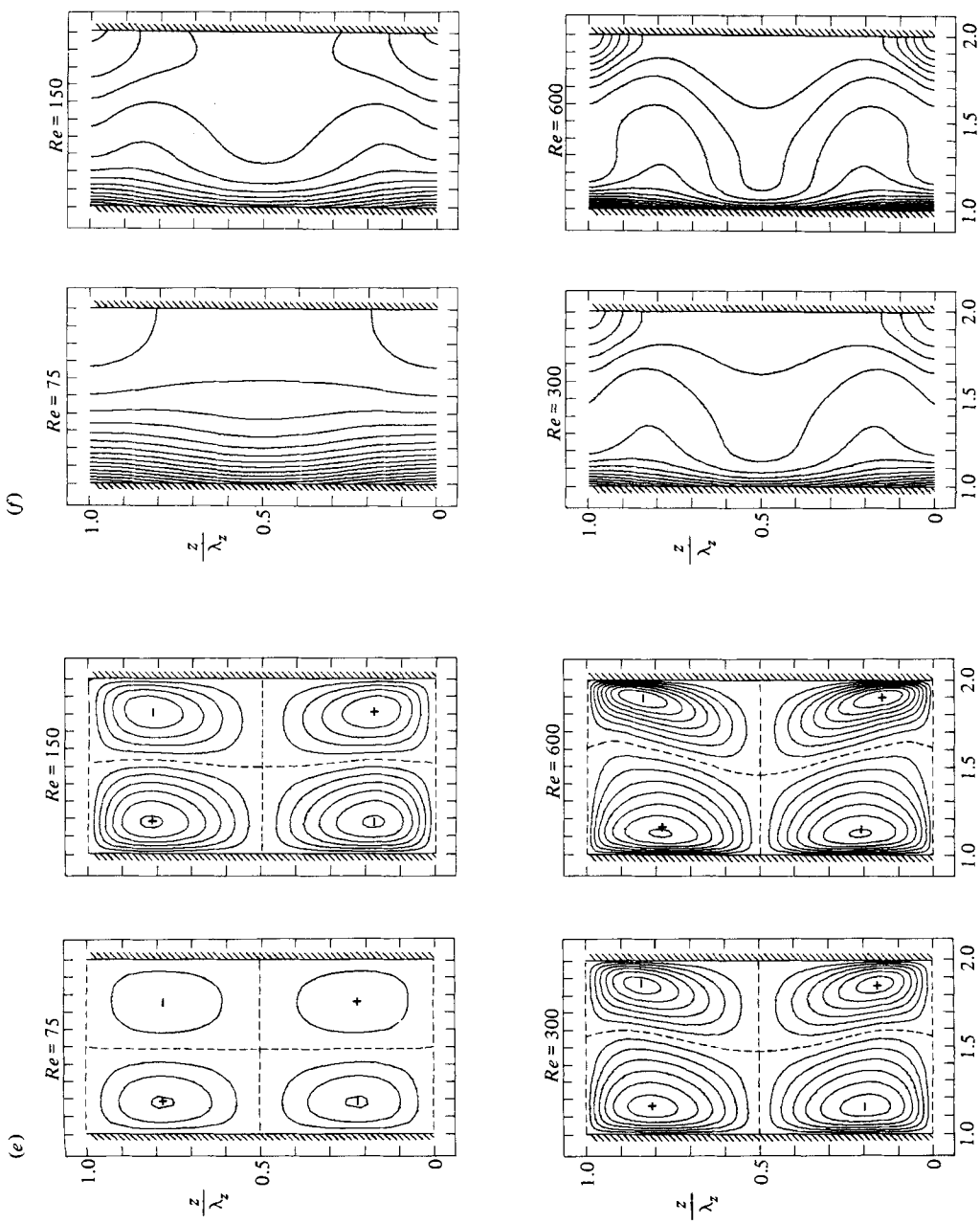


FIGURE 7. Isolines for Reynolds numbers $Re = 75, 150, 300, 600$: (*a*) $\psi$ (increment between lines $\Delta\psi = 0.008$); (*b*) $\omega$ ($\Delta\omega = 0.2$ for $Re = 75, 150$; $\Delta\omega = 0.4$ for $Re = 300$; $\Delta\omega = 0.8$ for $Re = 600$); (*c*) $u$ ($\Delta u = 0.025$); (*d*) $v$ ($\Delta v = 0.1$); (*e*) $w$ ($\Delta w = 0.025$); (*f*) $p$ ($\Delta p = 0.008$).

Burkhalter & Koschmieder 1973). The upper and lower boundaries of these plots ($z/\lambda_z = 0$ and 1) correspond to the centre of this jet that is directed towards the outer cylinder. Figures 7 ($a, b$) indicate that with increasing $Re$ the intensity of these radial jets, also called 'sources' (see Burkhalter & Koschmieder 1966) becomes stronger. Also, the width of the jet decreases, while the region where the flow is directed from the outer cylinder towards the inner cylinder (the so-called 'sink', see Burkhalter & Koschmieder 1966) increases accordingly (the centre is at $z/\lambda_z = \frac{1}{2}$). The build-up of the jetlike structure in the axial plane is also clearly exhibited in the contour plots for $u$ of figure 7 ($c$). Already for $Re = 75$ the region of the sink ($u < 0$) has grown at the expense of the region with the source ($u > 0$). From this point on, the sink regions still increase somewhat, and the contours become distorted considerably. But more obvious is the disproportionate growth of $u$ (increasing density of contour lines) in the source regions relative to that in the sink regions.

The drastic changes of the flow field with increasing Reynolds number become also particularly evident from consideration of the azimuthal velocity distribution (figure 7 $d$). For $Re$ just beyond critical, lines of constant $v$ would be practically straight lines parallel to the cylinder walls, with a spacing in $r$ that would increase only slightly from the inner to the outer cylinder. On the other hand, for $Re = 75$, the contour lines are already warped. The lines appear to be attracted by the inner cylinder in a region where the sink develops, while the symmetry about the cell boundary $z/\lambda_z = 0.5$ is preserved. This attraction of contour lines increases dramatically with growing $Re$. At $Re = 600$, the contour lines are practically concentrated at the inner cylinder and in the narrow band of the radial jet region. This suggests the development of a boundary-layer-type behaviour for the azimuthal velocity component. In addition, it is evident that a narrow jet in the azimuthal direction evolves at the same $z$-location where the radial jet occurs. There are only a few contour lines near the outer cylinder and in the sink region these protrude, with larger $Re$, more and more towards the inner cylinder. The centre regions of each cell become increasingly depleted of contour lines, which means that $v$ varies there very little relative to the strong changes near the cylinder walls. The implication of this is that at large $Re$ the fluid mass in the centre portion of each cell moves with almost constant velocity in the azimuthal direction.

The contour plots for the $w$-component in figure 7 ($e$) also provide good insight into the changes of the flow field as $Re$ increases. The extrema in the outer half of the gap are shifted more and more towards the outer wall and towards the source regions. This leads to the shocklike structure (suggested by Snyder & Lambert 1966) as $w$ changes across the cell boundaries $z/\lambda_z = 0$ and 1 from a negative extremum to a positive extremum and vice versa. However, the shocklike structure is more pronounced near the outer cylinder wall and somewhat less near the inner wall, while in the centre region of the gap it is practically non-existent. The contour lines in figure 7 ($f$) for the pressure (obtained by solution of the Poisson equation (9) with a reference pressure such that $p = 0$ at $z = 0$, $r = 0$) strongly support the existence of the jetlike structures. In the region where the radial jet (in the axial plane) impinges on the outer wall ($z/\lambda_z = 0$ and 1), the pressure increases strongly. However, it should be noted that the pressure increase is also at least partly due to the presence of the azimuthal jet. An excess pressure at the location of impingement was suggested by Snyder & Lambert; however, their attempt to verify this failed due to the difficulties in measuring the pressure.

All in all, the contour plots of figure 7 provide an excellent survey of the qualitative changes in the flow field when $Re$ increases. The quantitative differences that develop

for large $Re$ can be better observed from figure 8, however, where $u$, $v$, $w$, $\omega$ and $p$ are shown for various sections of the flow field and are compared with each other for the same four Reynolds numbers as before. For example, the jetlike flow development can be best observed in plots of $u$, $v$, $\omega$ and $p$ versus $z$, i.e. in figures 8($b$,$f$, $i$,$j$, $n$). For the radial jet, figure 8($b$) shows relatively large positive velocity components (directed towards the outer cylinder) in the jet region with a peak at the centre of the jet. In the sink region the (negative) velocity directed towards the inner cylinder is much smaller, with a relatively broad region where the velocity varies relatively little. The corresponding development of the $r$-distribution of the $u$-component at the centres of the jet and sink region is shown in figure 8($a$).

The development of the azimuthal jet can be observed very clearly in figure 8($f$), where the azimuthal velocity in the middle of the gap is plotted versus $z$. For the largest Reynolds number, $Re = 600$, there is a distinct plateau in the centre region of the cell where the azimuthal velocity is practically constant. From there, the velocity increases sharply in a narrow $z$-region and peaks at the same $z$-location as that at which the velocity profile of the radial jet has its maximum. In contrast, the decrease of velocity in the sink region occurs over a much broader region, with the minimum at $z/\lambda_z = 0.5$. The $r$-distribution of the azimuthal jet can be assessed by comparing figures 8($c$, $d$, $e$), which show the azimuthal velocity versus $r$ for various $z$-locations. Figures 8($d$, $e$) also exhibit the build-up of the boundary-layer-type behaviour (for the azimuthal velocity) at the inner cylinder which was already suggested by the contour plots of figure 7($d$). The velocity distribution in the cell centre (figure 8$d$) also indicates the development of a boundary layer at the outer cylinder, although somewhat weaker than at the inner cylinder. In the centre region between the two boundary layers, the azimuthal velocity changes relatively little for large Reynolds numbers. In view of the large changes near the inner and outer cylinder, this can be interpreted as a solid-body type motion in the azimuthal direction of the fluid mass in the centres of the cell.

The pressure distributions in figures 8($l$–$q$) clearly demonstrate the build-up of distinct peaks at the locations of the radial and azimuthal jets. This is particularly obvious in the distribution versus $z$ at the outer wall (figure 8$n$), where the pressure is practically constant except for the pronounced peak at the location where the radial jet impinges on the outer cylinder wall. Recalling the azimuthal velocity distributions of figure 8($c$,$f$), this pressure build-up is at least partly due to the increased pressure required to balance the centrifugal forces in the azimuthal jet. However, simple order-of-magnitude estimates have shown that by far the biggest contribution for the sharp pressure rise from the middle of the gap to the peak at the outer cylinder walls (see figure 8$o$) is due to the deceleration and impingement of the radial jet.

At this point, the question arises as to whether the flow field resulting from our calculations supports the theoretical model by Batchelor (see Donnelly & Simon 1960), which is based on the assumption that, for $Re \to \infty$, the secondary flow in the axial plane consists of an inviscid core surrounded by boundary layers. When comparing our results with this theory, one should keep in mind, however, that the highest Reynolds number for which numerical results were discussed in this paper was still only 600.

Batchelor's theory does not address the question of symmetry of the flow pattern of the Taylor cells in the axial plane. The present calculations display considerable asymmetry of the flow pattern (see figure 7) as the Reynolds number increases. Apart from the torque relationship, with which our results agree reasonably well (see §5.1), Batchelor's theory (Batchelor 1956) yields two important results: ($a$) in the core

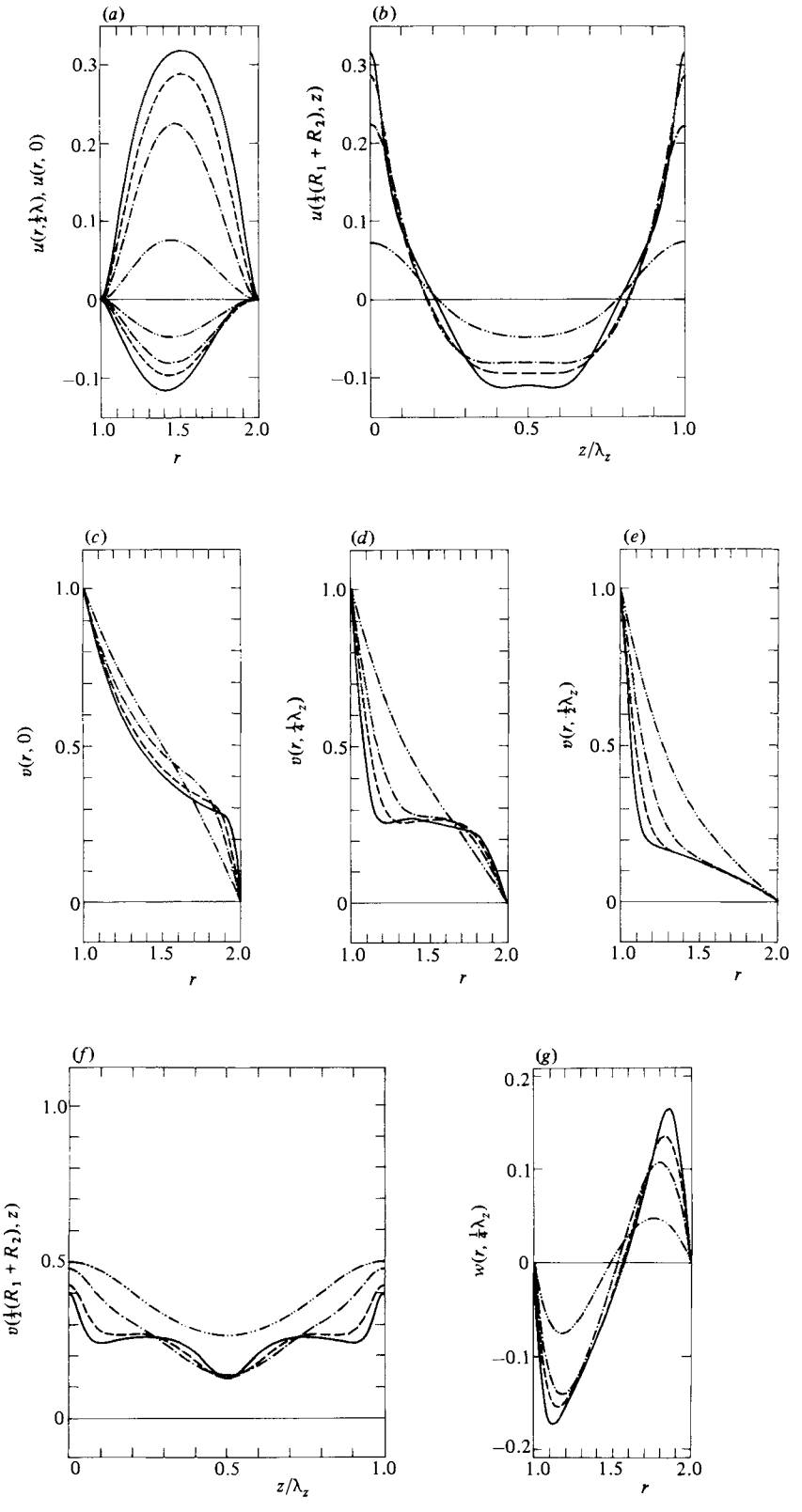


FIGURE 8(*a–g*). For caption see p. 44.

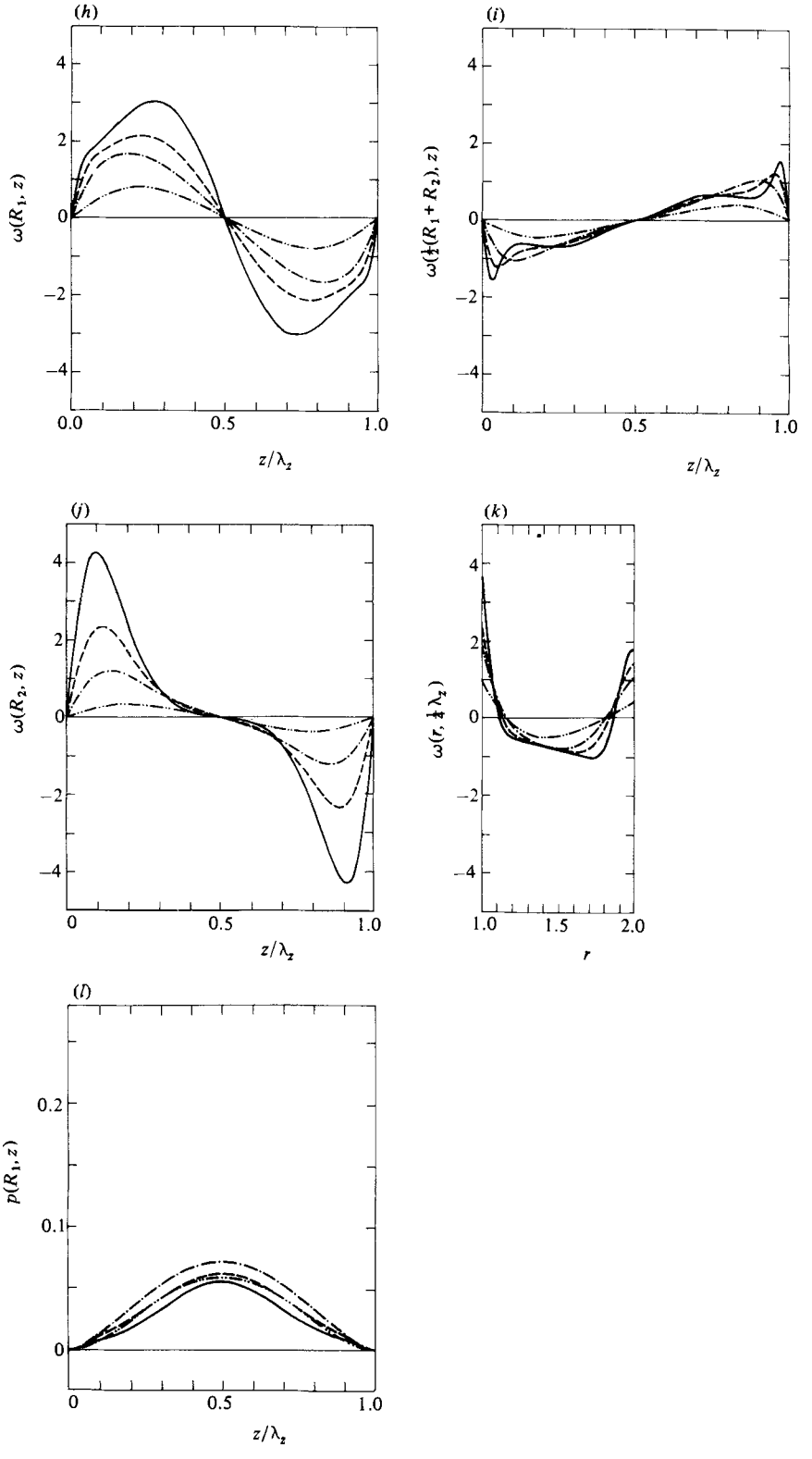


FIGURE 8(*h–i*). For caption see p. 44.

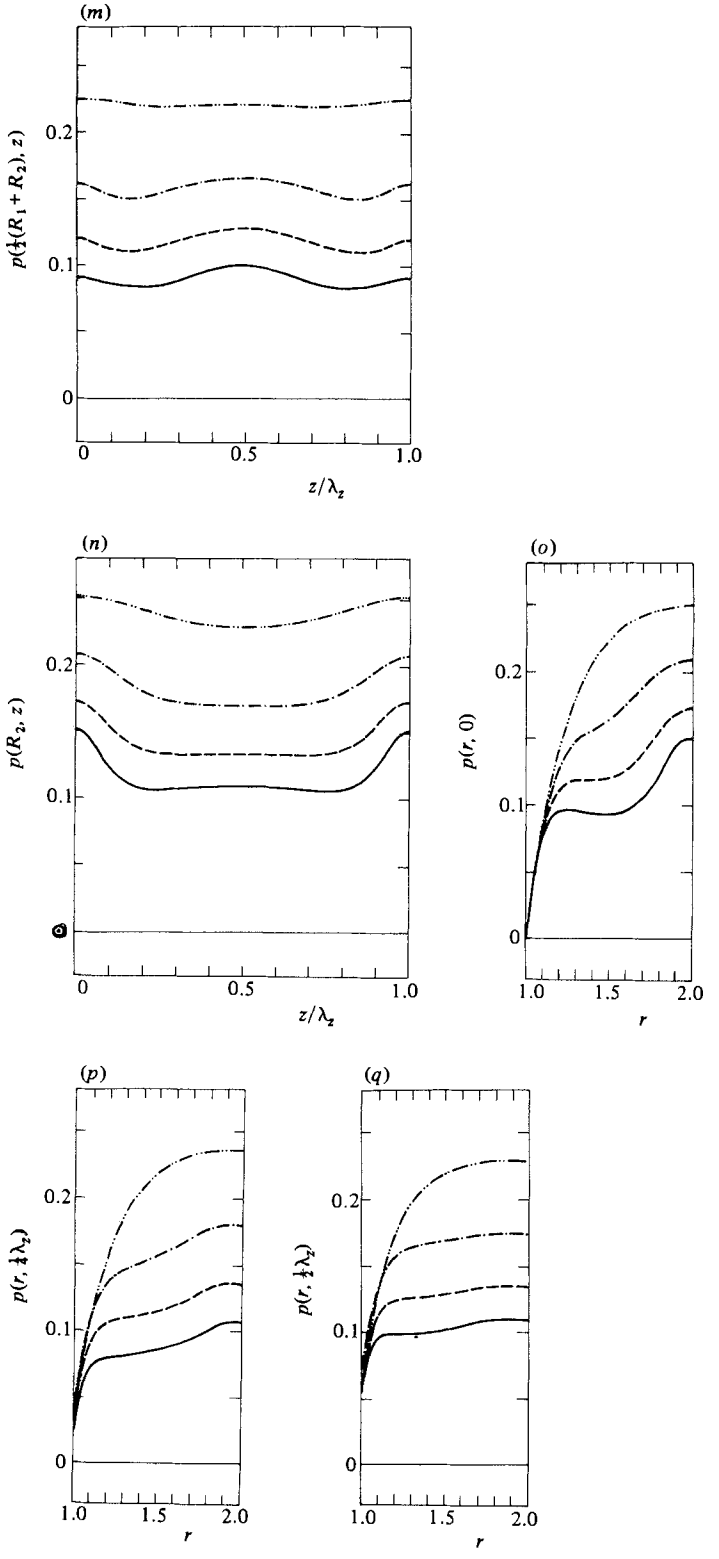


FIGURE 8. Variation of flow variables with $r$ and $z$ respectively, at representative locations $z$ and $r$ respectively: —··—·—··—, $Re = 75$; —·—·—·—, 150; – – –, 300; ———, 600.

region the azimuthal vorticity $\omega$ is proportional to $r$, and ($b$) in the core region the angular momentum $vr$ is constant. Our vorticity distributions with respect to $r$ for the centre of the cell in figure 8($k$) do indeed show a clear trend towards a linear variation of vorticity with $r$, and thus support result ($a$). On the other hand, the relationship $vr$ = constant is not quite as obvious from our results. For $Re = 600$, the curve of $v$ versus $r$ for the cell centre in figure 8($f$) shows a behaviour that could be interpreted as $vr$ = constant. However, the region where such a trend is prevalent is still too small for quantitative confirmation of relationship ($b$).

The assumption in the theoretical model that boundary layers exist along the inner and outer cylinder walls appears to be strongly justified in view of figures 8($g$, $k$). The vorticity distribution of figure 8($k$) indicates a development of the boundary layers along the inner and outer cylinder walls. For $Re = 600$, the vorticity is maximal (positive) at the inner and outer cylinder walls and drops off rapidly to negative values within thin layers near the walls. In contrast, in the core region vorticity is negative and varies linearly (as mentioned before) where the gradient is very small compared with the rapid variation in the wall boundary layers. The distributions of $w$ versus $r$ in figure 8($g$) also support the boundary-layer concept. The maxima and minima of the $w$-distributions move closer and closer towards the outer and inner cylinder walls, respectively, which leads to decreasing boundary-layer thicknesses as $Re$ increases.

### 5.3. *Harmonic components*

The profound changes of the Taylor-vortex flow when the Reynolds number is raised, as discussed in §5.2, are due to nonlinear effects. According to Stuart (1960), the three nonlinear effects are: ($a$) generation of harmonics (with respect to $z$) of the fundamental mode, ($b$) distortion of the mean motion, and ($c$) distortion of the fundamental mode.

At first, in the theoretical investigations of Stuart (1958) only the distortion of the mean motion was allowed for, and later in the study by Davey (1962) all three effects were included, except that the number of harmonics was limited to two (i.e. one higher harmonic). In the present study all three nonlinear effects are included, since the full nonlinear Navier–Stokes equations are solved numerically. By simple Fourier decomposition of the numerically obtained data all these nonlinear effects can be laid bare. The flow variables can be written as sums of Fourier components; for example, for the $u$- and $v$-components

$$u(r,z) = \sum_{j=0}^{\infty} \hat{u}_j(r) \sin\left[j\frac{2\pi}{\lambda z}z + \theta_{u_j}(r)\right], \tag{22a}$$

$$v(r,z) = v_C(r) + \sum_{j=0}^{\infty} \hat{v}_j(r) \sin\left[j\frac{2\pi}{\lambda z}z + \theta_{v_j}(r)\right], \tag{22b}$$

and correspondingly for the other flow variables. Subscript C in 22($b$) denotes the Couette flow. The Fourier amplitudes $\hat{u}_j(r)$, $\hat{v}_j(r)$ and $\hat{\omega}_j(r)$ can be determined from numerical Fourier analysis, where the number of Fourier components or harmonics that can be calculated is dependent on the accuracy, i.e. the number of grid points, used for the solution of the Navier–Stokes equations. For $j = 0$ the Fourier analysis yields a non-fluctuating term which corresponds to the (distorted) mean motion. For $j = 1$ the Fourier distribution corresponds to the (distorted) first harmonic (fundamental mode) and for $j = 2, 3, \ldots$ the corresponding other harmonics are obtained. Typical results are presented in figures 9–11.

For example, in figure 9 the Fourier amplitudes $\hat{v}_j$ and $\hat{\omega}_j$ are shown versus $Re$ in

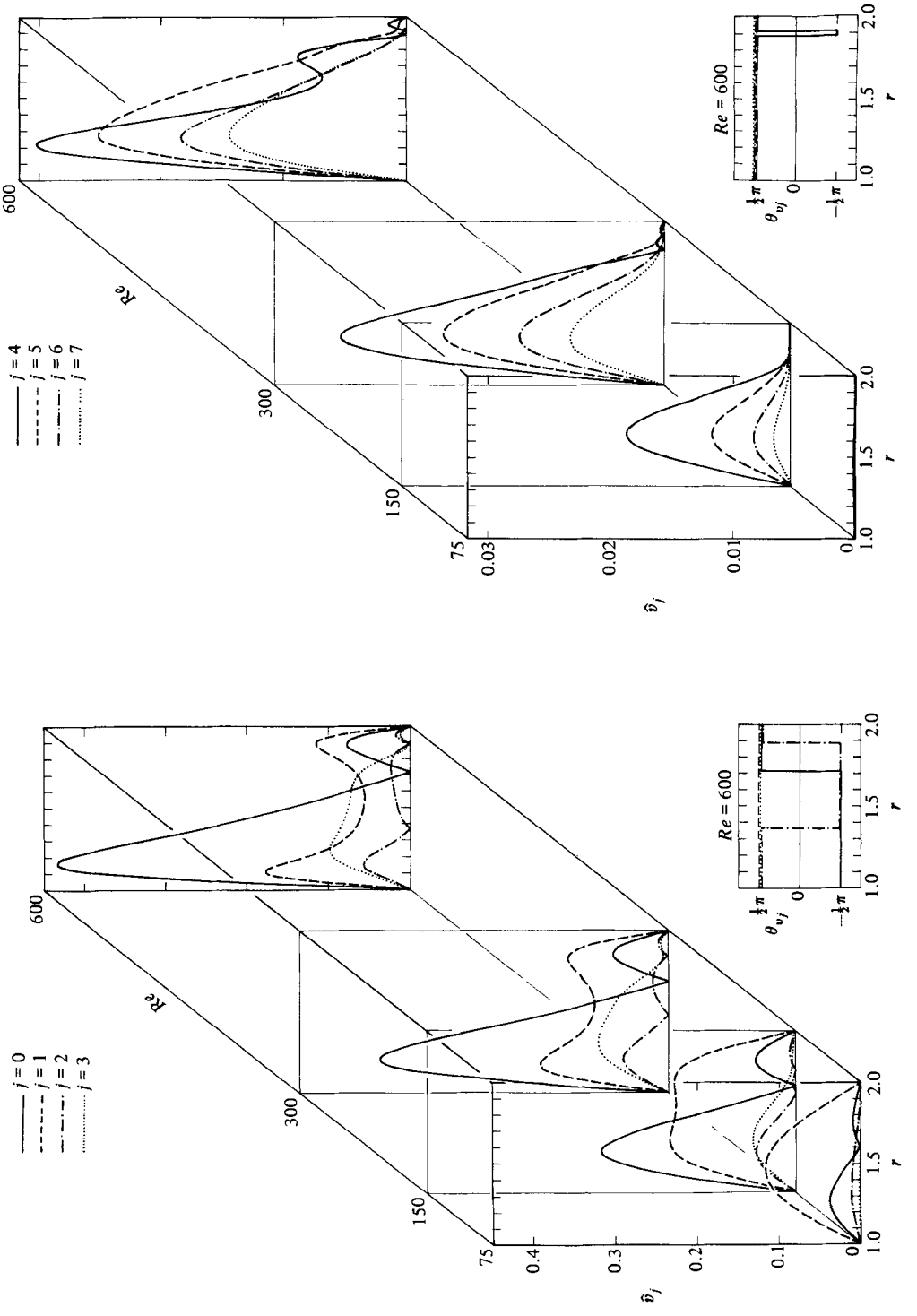


(a)

FIGURE 9(a). For caption see facing page.

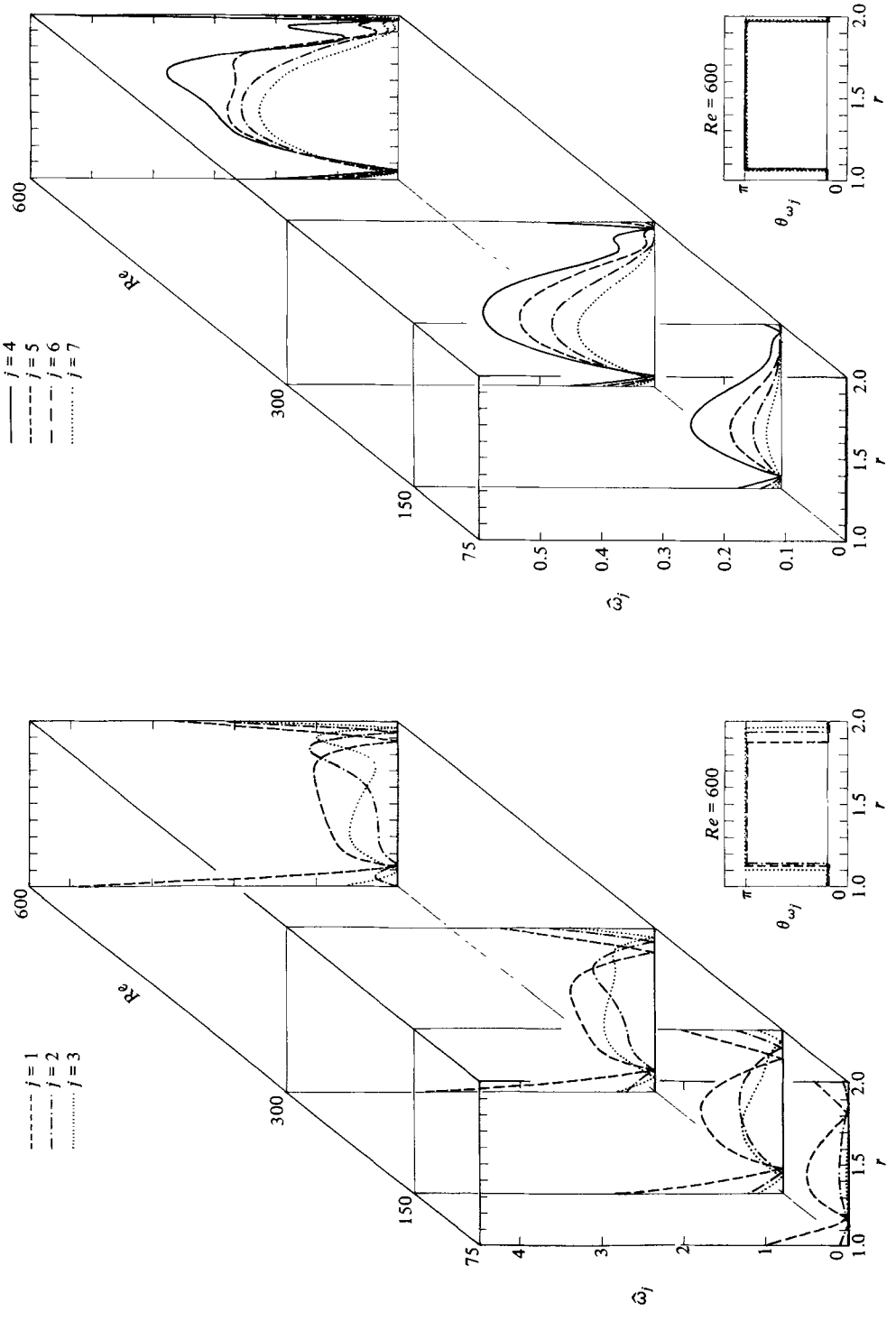


FIGURE 9. Harmonic components $\hat{v}_j(r)$ and $\hat{w}_j(r)$ for Reynolds numbers $Re = 75, 150, 300, 600$ (phae $\theta_{vj}$ and $\theta_{\omega j}$ for $Re = 600$ only). (*a*) harmonic components $\hat{v}_j, j = 0, 1, \ldots, 7$; (*b*) harmonic components $\hat{\omega}_j, j = 1, 2, \ldots, 7$.

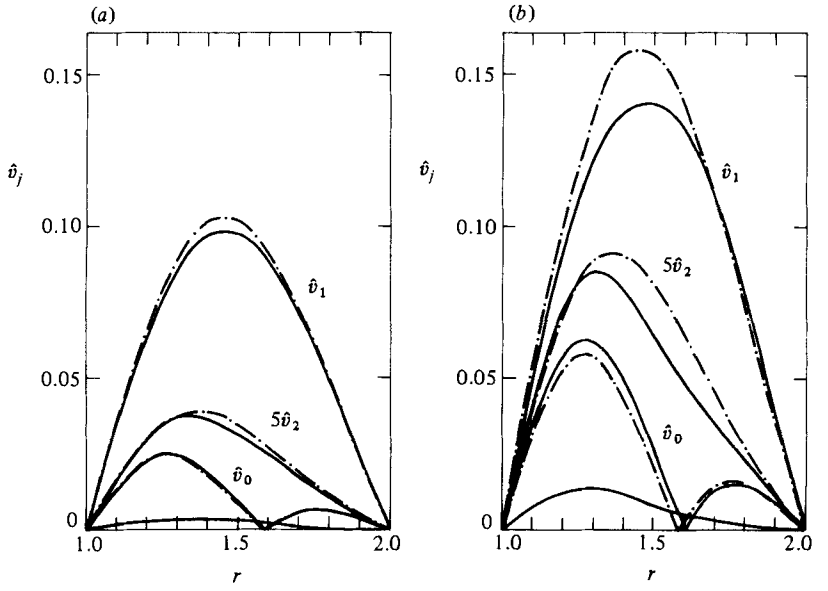


FIGURE 10. Harmonic components $\hat{v}_j$ versus $r$ for Reynolds numbers $Re = 72.5$ and $Re = 80$; comparison with stability theory: —·—·—, stability theory (Davey 1962); ——, present (Navier–Stokes solution). (*a*) $Re = 72.5$; (*b*) $Re = 80$.

quasi-perspective plots to elucidate the changes that the various harmonics undergo with increasing Reynolds number. As seen in figure 9(*a*), the change $\hat{v}_0 - v_C$ of the mean flow becomes considerable in magnitude with large $Re$. The shape of the distribution does not change very much, except that the peak near the inner cylinder (with advance velocity) grows slightly faster than that (with defect velocity) near the outer cylinder. (The phase-angle distribution with respect to $r$ is shown in these plots for the largest Reynolds number, $Re = 600$, only.) The fundamental mode, $j = 1$ (first harmonic), on the other hand, does not grow very much in absolute amplitude. Rather, there is a pronounced change of its shape. For small $Re$ ($Re = 75$) it has the shape of a half sine and with increasing $Re$ the gradients at the inner and outer cylinder become much bigger and a plateau develops ($Re = 150$) in the centre region of the gap. With further increase of $Re$, two distinct peaks develop near the inner and outer cylinder, while the plateau develops into a (sinking) valley. The second and third harmonics ($j = 2$, $j = 3$) grow rapidly for moderate supercritical $Re$ (between $Re = 75$ and 300) and then these harmonics change mainly with respect to their $r$-distributions. It should be noted that for large $Re$ the third harmonic in the centre region of the gap is larger in magnitude than the second harmonic and almost reaches the magnitude of the first harmonic.

For the higher harmonic components ($j = 4, \ldots, 7$) the changes with increasing $Re$ show up at first (up to about $Re = 300$) in a strong growth, with only minor changes in the shape of the $r$-distribution. There is practically no harmonic content in the region close to the outer wall. It is also obvious that growth is stronger the higher the harmonic, i.e. the $j = 4$ harmonic grows faster than the $j = 3$, etc. For example, at $Re = 600$ the maximum of the seventh harmonic is about 50 % of that of the fourth harmonic. In addition, for larger $Re$ ($Re \geqslant 300$) the shape of the $r$-distributions change considerably. This is most noticeable for the fourth harmonic, for which two maxima develop near the outer cylinder. Because of these changes of shape, there is an

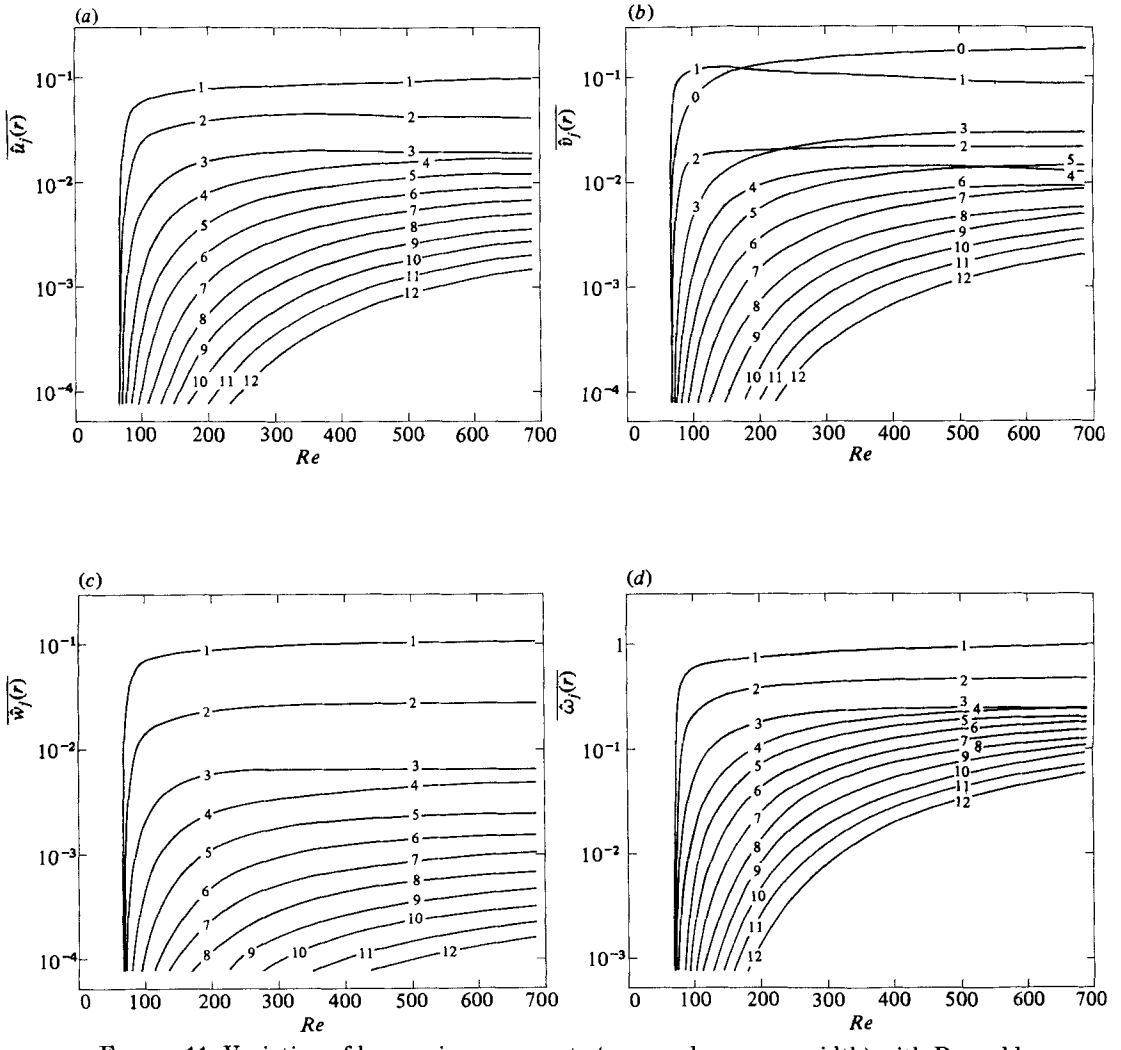


FIGURE 11. Variation of harmonic components (averaged over gap width) with Reynolds number: (*a*) $\overline{\hat{u}}_j$; (*b*) $\overline{\hat{v}}_j$; (*c*) $\overline{\hat{w}}_j$; (*d*) $\overline{\hat{\omega}}_j$.

extended region in the centre part of the gap, where the fifth harmonic considerably exceeds the fourth, and a smaller region where even the sixth and seventh are larger than the fourth.

The Fourier components for $\omega$ (figure 9*b*) show similar behaviour with respect to the growth of the harmonics for small supercritical $Re$ and with respect to the pronounced changes of the $r$-distribution for larger $Re$. The changes in the $r$-distribution are particularly noticeable for the $j = 2$ and $j = 3$ components and for the $j = 4$ and $j = 5$ components. It is also obvious that with increasing $Re$ the higher harmonics ($j = 4$) are more and more of the same order of magnitude for a wide region of the gap except near the inner and outer cylinder (see e.g. the figures for $Re = 600$).

The growth and the strong changes in the amplitude distributions and the growing number of harmonics that become relevant when $Re$ increases, explain the deviation between the analytical results (Davey 1962) for the torque (figure 4) and the $u$- and $v$-components (figure 5) and the Navier–Stokes results. Davey's analysis is based,

after all, specifically on an expansion about the critical Reynolds number and only 2 harmonic components were allowed for. A comparison of the Fourier components for the $v$-component obtained by Davey with our Navier–Stokes calculations in figure 10 clearly reveals the deviations even for moderate supercritical $Re$. For $Re = 72.5$ in figure 10 ($a$) the deviations are only minor, whereas for $Re = 80$ (in figure 10$b$) the deviations, especially in the centre region of the gap, become more substantial.

Figure 9 provides a qualitative survey of how nonlinearity, i.e. increasing Reynolds number, leads to the creation and growth of harmonics and how the distributions of the harmonic components can change. It has also become clear that the local growth of the harmonics with $Re$ is strongly dependent on the $r$-coordinate and on the flow variable in consideration. To be able to provide consistent comparison of the growth curves for different harmonics, the amplitude distributions for the harmonics were averaged over the gap width; for example, for $u$,

$$\overline{\hat{u}_j(r)} = \frac{1}{R_2 - R_1} \int_{R_1}^{R_2} \hat{u}_j(r)\, \mathrm{d}r. \tag{23}$$

The development of these average amplitudes with $Re$ is shown in figure 11 for the first twelve harmonics. Now it becomes even more obvious how the higher harmonics come in rapidly when $Re$ increases. Typically, the lower the harmonic the stronger is its initial growth. But, more important, beyond the strong amplification there is a rapid levelling off with an obvious asymptotic behaviour, which indicates a saturation mechanism. Thus, for larger $Re$ the lower harmonics remain practically constant while higher harmonics still grow rapidly with $Re$. For the azimuthal velocity component in figure 11 ($b$) the fundamental mode ($j = 1$) even overshoots and then approaches a constant value. Also, the odd-numbered components $j = 3, 5, 7, \ldots$ overtake their corresponding preceding even-number components $j = 2, 4, 6, \ldots$ .

Thus for larger $Re$ an unexpectedly large number of harmonics contribute to the total solution. For example, for vorticity (figure 11$d$) at the largest Reynolds number calculated, the $j = 12$ component still has more than 20 % of the amplitude of $j = 3$ component! This fact is a possible explanation why, in the comparison of our calculations with those of Rogers & Beard for $Re = 150$ (figure 6), a slight deviation starts to develop at the jet location ($z = 0$). Rogers & Beard used six components in their calculations. For the $u$-component in figure 11 ($a$), for example, at $Re = 150$ the $j = 7$ harmonic is still approximately 50 % of the $j = 6$ harmonic in amplitude, and even the $j = 9$ harmonic is still 10 % of the $j = 6$ component. And, recalling figure 9, local differences between higher and lower components may be even less, or higher harmonics can locally be even larger than the lower ones.

## 6. Conclusion

An implicit finite-difference method of fourth-order accuracy has been employed to investigate the Taylor-vortex flow in a wide gap ($R_1/R_2 = 0.5$) for large supercritical Taylor numbers. The numerical results presented in this paper provide evidence of considerable changes in the flow field as the Taylor number is increased from low to high supercritical Taylor numbers up to $100Ta_c$. Detailed analysis of various flow variables, such as velocity components, stream function, vorticity and pressure, strongly supports the concept of an evolving jetlike (shocklike) structure when the Taylor number is increased. A good indication of this is found, in particular, in the pressure peaks that develop on the outer cylinder wall at the locations of jet

impingement. For large supercritical Taylor numbers the flow exhibits a boundary-layer-type structure at the inner and outer cylinder walls for both the flow in the axial plane and the flow in the azimuthal direction. In contrast, the flow in the core region in the axial plane behaves as essentially inviscid. The azimuthal velocity varies very little in the centre region of the cell, which can be interpreted as an approximate solid-body-type motion in the azimuthal direction of the fluid in this region. Spectral decomposition of the computed flow quantities has shown that a relatively large number of higher harmonic components are required to resolve these strong changes of the flow field for large Taylor numbers.

The authors would like to thank Dr D. Coles, California Institute of Technology, Dr J. T. Stuart, Imperial College, and Dr E. J. Kerschen, University of Arizona, for their interest in this work and their valuable comments. This research was supported by the Deutsche Forschungsgemeinschaft under Contract Fa 117/2-1.

## REFERENCES

BATCHELOR, G. K. 1956 On steady laminar flow with closed streamlines at large Reynolds number. *J. Fluid Mech.* **1**, 177–190.

BOOZ, O. 1980 Numerische Lösung der Navier–Stokes Gleichungen für Taylor-Wirbelströmungen im weiten Spalt. Dissertation, Universität Stuttgart.

BURKHALTER, J. D. & KOSCHMIEDER, E. L. 1973 Steady supercritical Taylor vortex flow. *J. Fluid Mech.* **58**, 547–560.

BURKHALTER, J. D. & KOSCHMIEDER, E. L. 1974 Steady supercritical Taylor vortices after sudden starts. *Phys. Fluids* **17**, 1929–1935.

CHANDRASEKHAR, S. 1961 *Hydrodynamic and Hydromagnetic Stability.* Clarendon.

COLE, J. A. 1976 Taylor-vortex instability and annulus-length effects. *J. Fluid Mech.* **75**, 1–15.

COLES, D. 1965 Transition in circular Couette flow. *J. Fluid Mech.* **21**, 385–425.

DAVEY, A. 1962 The growth of Taylor vortices in flow between rotating cylinders. *J. Fluid Mech.* **14**, 336–368.

DAVEY, A., DIPRIMA, R. C. & STUART, J. T. 1968 On the instability of Taylor vortices. *J. Fluid Mech.* **31**, 17–52.

DIPRIMA, R. C. & ROGERS, E. H. 1969 Computing problems in nonlinear hydrodynamic stability. In *High Speed Computing in Fluid Dynamics: Phys. Fluids Suppl.* II, 155–165.

DONNELLY, R. J. 1958 Experiments on the stability of viscous flow between rotating cylinders, I. Torque measurements. *Proc. R. Soc. Lond.* A **246**, 312–325.

DONNELLY, R. J. & SIMON, N. J. 1960 An empirical torque relation for supercritical flow between rotating cylinders. *J. Fluid Mech.* **7**, 401–418.

EAGLES, P. M. 1974 On the torque of wavy vortices. *J. Fluid Mech.* **62**, 1–9.

FASEL, H. 1974 Untersuchungen zum Problem des Grenzschichtumschlages durch numerische Integration der Navier–Stokes-Gleichungen. Dissertation, Universität Stuttgart.

FASEL, H. 1976 Investigation of the stability of boundary layers by a finite difference model of the Navier–Stokes equations. *J. Fluid Mech.* **78**, 355–383.

JONES, C. A. 1981 Nonlinear Taylor vortices and their stability. *J. Fluid Mech.* **102**, 249–261.

KIRCHGÄSSNER, K. 1961 Die Instabilität der Strömung zwischen zwei rotierenden Zylindern gegenüber Taylor-Wirbeln für beliebige Spaltbreiten. *Z. angew. Math. Phys.* **12**, 14–29.

KIRCHGÄSSNER, K. 1966 Verzweigungslösungen eines stationären hydrodynamischen Randwertproblems. Habilitationsschrift, Universität Freiburg.

KIRCHGÄSSNER, K. & SORGER, P. 1969 Branching analysis for the Taylor problem. *Q. J. Mech. Appl. Maths* **22**, 183–209.

KOGELMAN, S. & DIPRIMA, R. C. 1970 Stability of spatially periodic supercritical flows in hydrodynamics. *Phys. Fluids* **13**, 1–11.

MALKUS, W. V. R. & VERONIS, G. 1958 Finite amplitude cellular convection. *J. Fluid Mech.* **4**, 225–260.

MEYER, K. A. 1967 Time-dependent numerical study of Taylor vortex flow. *Phys. Fluids* **10**, 1874–1879.

MEYER, K. A. 1969 Three-dimensional study of flow between concentric rotating cylinders. In *High Speed Computing in Fluid Dynamics: Phys. Fluids Suppl.* II, 165–170.

MEYER-SPASCHE, R. & KELLER, H. B. 1980 Computations of the axisymmetric flow between rotating cylinders. *J. Comp. Phys.* **35**, 100–109.

NAKAYA, C. 1974 Domain of stable periodic vortex flows in a viscous fluid between concentric circular cylinders. *J. Phys. Soc. Japan* **36**, 1164–1173.

PARK, K. & DONNELLY, R. J. 1980 Work in progress reported at the Division of Fluid Mechanics – American Physical Society Meeting, Cornell University.

REYNOLDS, W. C. & POTTER, M. C. 1967 A finite-amplitude state-selection theory for Taylor-vortex flow. *Stanford University Paper.*

ROACHE, P. J. 1976 *Computational Fluid Dynamics.* Hermosa.

ROGERS, E. H. & BEARD, D. W. 1969 A numerical study of wide-gap Taylor vortices. *J. Comp. Phys.* **4**, 1–18.

SCHULTZ-GRUNOW, F. & HEIN, H. 1956 Beitrag zur Couetteströmung. *Z. Flugwiss.* **4**, 28–30.

SCHWARZ, K. W., SPRINGETT, B. E. & DONNELLY, R. J. 1964 Modes of instability in spiral flow between rotating cylinders. *J. Fluid Mech.* **20**, 281–289.

SNYDER, H. A. 1969 Wave number selection at finite amplitude in rotating Couette flow *J. Fluid Mech.* **35**, 273–298.

SNYDER, H. A. & LAMBERT, R. B. 1966 Harmonic generation in Taylor vortices between rotating cylinders. *J. Fluid Mech.* **26**, 545–562.

STRAWBRIDGE, D. R. & HOOPER, G. T. J. 1968 Numerical solutions of the Navier–Stokes equations for axisymmetric flows. *J. Mech. Engng. Sci.* **10**, 389–401.

STUART, J. T. 1958 On the nonlinear mechanics of hydrodynamic stability. *J. Fluid Mech.* **4**, 1–21.

STUART, J. T. 1960 On the nonlinear mechanisms of wave disturbances in stable and unstable parallel flows. *J. Fluid Mech.* **9**, 353–370.

STUART, J. T. 1971 Nonlinear stability theory. *Ann. Rev. Fluid Mech.* **3**, 347–370.

TAYLOR, G. I. 1923 Stability of a viscous liquid contained between two rotating cylinders. *Phil. Trans. R. Soc. Lond.* A **223**, 289–343.

VELTE, W. 1966 Stabilität und Verzweigung stationärer Lösungen der Navier–Stokesschen Gleichungen beim Taylor-Problem. *Arch. Rat. Mech. Anal.* **22**, 1–14.